



Cite this: *Phys. Chem. Chem. Phys.*,
2016, 18, 28704

Neural network molecular dynamics simulations of solid–liquid interfaces: water at low-index copper surfaces†

Suresh Kondati Natarajan and Jörg Behler*

Solid–liquid interfaces have received considerable attention in recent years due to their central role in many technologically relevant fields like electrochemistry, heterogeneous catalysis and corrosion. As the chemical processes in these examples take place primarily at the interface, understanding the structural and dynamical properties of the interfacial water molecules is of vital importance. Here, we use a first-principles quality high-dimensional neural network potential built from dispersion-corrected density functional theory data in molecular dynamics simulations to investigate water–copper interfaces as a prototypical case. After performing convergence tests concerning the required supercell size and water film diameter, we investigate numerous properties of the interfacial water molecules at the low-index copper (111), (100) and (110) surfaces. These include density profiles, hydrogen bond properties, lateral mean squared displacements and residence times of the water molecules at the surface. We find that in general the copper–water interaction is rather weak with the strongest interactions observed at the Cu(110) surface, followed by the Cu(100) and Cu(111) surfaces. The distribution of the water molecules in the first hydration layer exhibits a double peak structure. In all cases, the molecules closest to the surface are predominantly allocated on top of the metal sites and are aligned nearly parallel with the oxygen pointing slightly to the surface. The more distant molecules in the first hydration layer at the Cu(111) and Cu(100) surfaces are mainly found in between the top sites, whereas at the Cu(110) surface most of these water molecules are found above the trenches of the close packed atom rows at the surface.

Received 17th August 2016,
Accepted 29th September 2016

DOI: 10.1039/c6cp05711j

www.rsc.org/pccp

1 Introduction

Solid–liquid interfaces (SLI) are omnipresent in nature as well as in many technological applications and thus have been studied extensively in recent years.^{1–6} There are many important examples, like electrode–electrolyte interfaces in electrochemical energy storage and conversion⁷ and catalyst–solvent interfaces in heterogeneous catalysis. Among the solvents used in technologically relevant SLIs, water takes a prominent role. In spite of its simple chemical composition it is a very special liquid and its understanding has challenged researchers for many years.^{8–11} In case of SLIs the situation is even more complicated as the presence of the surface introduces density anisotropies and many other interesting phenomena in the interfacial region. The concept of the double layer in electrochemical systems as introduced by Helmholtz in 1853 is a classical and still little understood example.¹² It is widely believed that this double layer mediates

the charge transfer between electrode and electrolyte solution and understanding its structure is important to unravel its chemistry.^{13–15} Apart from acting as a solvent, water molecules may also dissociate and react with the surface forming even more complex structural patterns.

In order to study SLIs experimentally, techniques that are sensitive to the interfacial region but not to the bulk liquid or bulk substrate are required, and theoretical calculations have been found very useful to interpret the experimental findings.^{16–18} For example, scanning tunnelling microscopy (STM) together with density functional theory (DFT) calculations enabled studying molecular and monolayer adsorption of water on metal surfaces under ultra high vacuum conditions.^{19–25} From adsorption studies of water monolayers on close packed transition metal surfaces, the widely believed ice-like bilayer formation is still controversially discussed.^{26–30}

Ambient pressure X-ray photo electron spectroscopy,³¹ *in situ* X-ray diffraction³² and atomic force microscopy³³ have allowed *in situ* studies on solid–liquid interfaces. Optical second harmonic generation and vibrational sum frequency generation^{34,35} are state-of-the-art experimental techniques that have the ability to probe SLIs selectively. Recently, nano-ultrasonic sound waves

Lehrstuhl für Theoretische Chemie, Ruhr-Universität Bochum, D-44780 Bochum, Germany. E-mail: joerg.behler@theochem.ruhr-uni-bochum.de;

Fax: +49 234 32 14045; Tel: +49 234 32 26749

† Electronic supplementary information (ESI) available. See DOI: 10.1039/c6cp05711j

have also been employed in understanding the structure and properties of interfacial water.³⁶

Theoretical studies of SLIs are usually based on molecular dynamics (MD) simulations as, in contrast to the gas–surface interface, solid–liquid interfaces require sampling of the rapidly fluctuating solvent molecules, making simulations computationally very demanding. The most accurate tool for this purpose is *ab initio* MD³⁷ relying on the calculation of the energy and forces on-the-fly employing DFT. To date, a series of *ab initio* MD simulations have been performed on SLIs.^{14,38–52} Due to the high computational costs, SLIs have also been studied by more approximate methods like the DFT-3D reference interaction site model (RISM) scheme,⁵³ tight binding,⁵⁴ first principles reaction modelling⁵⁵ and quantum mechanics/molecular mechanics (QM/MM) approach.⁵⁶ Further, implicit solvation models are available to study SLIs treating the solvent molecules as a continuum field thereby reducing the number of atoms treated quantum mechanically.⁵⁷ Apart from MD, many DFT studies have been carried out on the adsorption of smaller amounts of water, from a single water molecule to several monolayers.^{17,27,43,58–73}

In the present work we study the water–copper interface as a prototypical example for SLIs. Michaelides *et al.*⁵⁸ in 2003 reported that a water molecule on Cu(111) surface preferentially adsorbs on the atop metal site with an orientation of the molecular plane almost parallel to the surface. They also mention that the water molecule binds rather weakly to the Cu(111) surface compared to other close packed transition metal surfaces like Pt(111), Pd(111), Rh(111) and Ru(0001). A similar observation has also been made earlier by Landman and co-workers⁷⁴ for a water molecule adsorbed at the Cu(100) surface studied in a cluster approach. Michaelides and Morgenstern²⁰ studied small nanoclusters and bilayers of water on the Cu(111) surface using STM and DFT and concluded that there is a competition between the water–water interaction and the water–substrate interaction and this competition determines the structure of the bilayer. Ito and Yamazaki⁷⁵ found that the contact layer water molecules are likely to form a close packed-like highly disordered structure on the Cu(111) surface. A similar observation has been made by Mehlhorn and Morgenstern,⁷⁶ who studied the non-wetting behaviour of water on Cu(111) and found that water forms complex 3D clusters instead of a simple ice structure.

The nature of water adsorption at metal surfaces may be very different due to varying inter-atomic distances and wetting properties of the metal surfaces. Tang and Chen⁶⁶ have investigated the adsorption of water monomers on several low-index copper surfaces using DFT and found that the adsorption energy increases in the following surface order, Cu(111) < Cu(100) < Cu(110). Ren and Meng⁶⁷ studied the structure of a water monomer and water over-layers on copper surfaces and discovered that there is a high tendency of dissociation and desorption of water molecules at close packed Cu(111) and Cu(100) surfaces, while dissociative adsorption is preferred at Cu(110) surface. Yamada *et al.*⁷⁷ found one dimensional chain growth on the Cu(110) surface along the loosely packed row

with the help of STM and similar findings have been reported by other researchers using DFT calculations.^{21,78} Forster *et al.*²⁴ found from a monolayer water adsorption study on Cu(110) that the concept of ice-like bilayer does not hold as the water molecules dissociate and form complicated hydroxyl layers.

To understand SLIs, water over-layers beyond the monolayer have to be sampled.^{6,14} Izvekov *et al.*⁴¹ in 2001 performed *ab initio* MD simulation on Cu(110)–water interface and discovered that the water molecules close to the surface prefer atop metal sites (like at Cu(111)³⁹) and form a bilayer structure which is not ice-like. They report less than full monolayer coverages in the contact layer of the water molecules and did not observe any spontaneous dissociation. Schnur and Groß⁴⁴ reported that water bilayer structures on noble metal surfaces are unstable at room temperatures. Nadler and Sanz in 2011⁴⁸ observed in MD simulations of liquid water on Cu(111) surface that the water molecules in the first layer adsorb O-down and the H-bond network is weaker upon adsorption on the close packed surface. It remains to be seen if this behaviour is common for different low index surfaces of copper.

Due to the high costs of *ab initio* MD, several more efficient interatomic potentials for describing SLIs have been proposed that enable performing extended simulations of larger systems.^{79–86} These potentials are usually constructed employing physical models of atomic interactions. Machine learning (ML) potentials offer an alternative approach, in which the potential energy surface (PES) is built without any constraints on the functional form using electronic structure data. ML has paved a novel way to construct PES and in recent years a number of different ML schemes have become available⁸⁷ including Gaussian approximation potentials,⁸⁸ artificial neural networks⁸⁹ and non-linear regression models.⁹⁰ Still, to date they have not been applied to simulations of SLIs.

In the present work, we investigate the structural and dynamical properties of the interfacial water molecules at several water–copper interfaces by molecular dynamics simulations employing a neural network (NN) potential to provide the required energies and forces at the dispersion corrected generalized gradient approximation (GGA) DFT level. After the identification of the converged system size, we unravel a number of physical properties of water molecules at the low index Cu(111), Cu(100) and Cu(110) surfaces including water probability densities, molecular orientations, hydrogen-bond lifetimes and residence times at the surface to obtain systematic insights into the interfacial water layers.

2 High-dimensional neural network potentials

In recent years several approaches have been introduced to construct interatomic potentials employing machine learning techniques.⁸⁷ Among the first of these methods artificial neural networks^{91,92} have been proposed for the development of DFT PESs by Blank *et al.*⁹³ in 1995 to describe the interaction of diatomic molecules with solid surfaces, and in the following

years many other systems have been addressed by numerous research groups as summarized in several reviews.^{94,95}

NNs are particularly apt for the expression of multi-dimensional real-valued functions like PESs, since in principle they enable an exact representation.^{96,97} Apart from providing energies and forces in close numerical agreement with the underlying reference electronic structure values, they offer further advantages like computational efficiency, the ability to describe chemical reactions, and the applicability to a wide range of systems without changes in the functional form, which is independent of the nature of the atomic interactions and the nuclear arrangements.

In the present work we use a generalized NN approach for high-dimensional PESs, which has been introduced by Behler and Parrinello in 2007.⁸⁹ In this method, the total potential energy E is expressed as a function of the positions of all N_{atom} atoms in the system in form of a sum of environment-dependent atomic energy contributions E_i

$$E = \sum_{i=1}^{N_{\text{atom}}} E_i. \quad (1)$$

The atomic environments are defined by a cutoff radius, which needs to be converged to include all energetically relevant interactions. Typically, cutoff values between 6 and 10 Å are sufficient to achieve the desired precision of a few meV per atom for total energies. The normalization of the error “per atom” ensures size-consistency and thus enables the combination and comparison of structures differing in the number of atoms. All neighboring atoms inside the resulting cutoff spheres enter the corresponding atomic energies E_i . The relative positions of these atoms with respect to the central atom are described by a vector of atom-centered many-body symmetry functions,⁹⁸ which takes into account the rotational, translational and permutational invariance of the potential energy⁹⁹ and can be directly calculated from the Cartesian coordinates of the atoms.

For each element in the system an individual atomic NN is constructed consisting of a number of artificial neurons arranged in one or more hidden layers as well as of a set of weight parameters, which is optimized to reproduce the DFT energies of a data base of known reference structures. Also the forces, which are obtained from the analytic gradients of the NN energy, are used for the optimization process. The element-specific atomic NNs are then replicated and evaluated for each atom of the respective element in the system. High-dimensional neural network potentials of this type have been constructed in the past for numerous systems including several subsystems relevant for the present study like copper,^{100,101} water clusters,^{102,103} liquid water^{104,105} and electrolytes.¹⁰⁶ The technical details about the method and a list of potentials developed to date can be found in two recent reviews.^{99,107}

3 Computational details

The DFT reference calculations have been carried out using the Vienna *Ab initio* Simulation Package (VASP)¹⁰⁸ version 5.3.

The exchange and correlation contributions of the electronic energy have been computed employing the RPBE functional, which is a GGA functional developed by Hammer *et al.*¹⁰⁹ The electron-core interaction is pseudized by projector augmented waves¹¹⁰ (PAWs) with a plane wave basis set energy cutoff of 700 eV for the valence electrons. PBE-based PAW potentials from the VASP pseudopotential library are used (core radii of 2.3 Å, 1.1 Å and 0.8 Å for Cu, O, and H, respectively).¹¹¹ In several recent studies dispersion-corrected DFT has been found to be crucial for a reliable description of bulk water^{104,112–114} as well as for water at metal surfaces.^{115–119} Consequently, semi-empirical dispersion corrections based on Grimme’s D3¹²⁰ method with zero damping as computed with DFT-D3 v3.1 code¹²¹ have been added to the RPBE energies and forces before training the NN potential, as the combination of the RPBE functional and the D3 method has been demonstrated to provide a reasonable description of water clusters and liquid water.^{103,104,113,122} The three body contributions to the D3 dispersion energy are not included in the reference calculations. Since the NN fitting process can be complicated by numerical noise in the reference data, which could arise from underconverged k -point grids, for all calculations k -points corresponding in density to a $12 \times 12 \times 12$ grid for the four-atom fcc unit cell of copper have been used. Only a single k -point has been taken into account along the very long lattice parameter normal to the metal surface in the slab calculations.

Generating the reference geometries is a crucial component in the construction of any ML-based potential, because, due to the lack of a physically derived functional form, the PES will have the correct physical shape only if all relevant parts of the configuration space are covered. Specifically, all subsystems like bulk water, bulk copper and the interface must be well represented in the data set to ensure that the ternary NN PES for the Cu/O/H system does describe all relevant parts of the system, like bulk water, with an accuracy comparable to that of on-the-fly *ab initio* MD. This is mandatory to decouple the two interfaces in our slab setup by a sufficiently thick water region in the center that possesses the same properties as pure bulk water.

To achieve this goal, we have carried out periodic DFT calculations for bulk copper, bulk liquid water and ice as well as a wide range of copper-water interface structures of the investigated surfaces including ordered and distorted configurations. Further, snapshots from MD simulations in a temperature range between 300 and 800 K have been added to include highly repulsive structures with close atomic encounters. The MD trajectories have been generated by Born–Oppenheimer *ab initio* MD simulations with reduced k -point sets and using preliminary NN potentials. From these trajectories uncorrelated structures have been selected, for which then fully converged single point calculations have been carried out to obtain a consistent reference set for training the NN. Finally, some cuprous oxide (Cu_2O) structures have also been included in case similar atomic environments would be formed during the simulations employing the NN potential.

Using this reference set, the high-dimensional NN potential has been constructed employing our in-house program RuNNer.¹²³

For this purpose, the available data has been randomly split into a training set (90%) to determine the weight parameters of the atomic NNs and an independent test set (10%) to validate the transferability of the potential to structures not used in the optimization process. Reference structures have been extracted from MD simulations using large time intervals between them to avoid structural correlations. Thus the test set geometries provide a measure for the predictive power of the potential. Only if the root mean squared errors (RMSEs) of the energies and of the forces of both sets are similar, a reliable potential has been obtained. Several NN architectures have been tested for the atomic NNs to identify the topology providing the best representation of the PES. These architectures include an input layer with one neuron per symmetry function to provide the structural information describing the atomic environments to the atomic NNs, usually two hidden layers containing various numbers of neurons to adjust the flexibility of the NNs for representing the atomic energy contributions, and an output layer with a single neuron yielding the energy contribution of the respective atom. For all neurons in the hidden layers the hyperbolic tangent has been used as activation function, while a linear function has been applied in the output layer. The definitions of the symmetry functions describing the atomic environments for all elements are listed in the ESI,[†] Section 1.

In the training process, the weight parameters are optimized employing the gradient-based Kalman filter¹²⁴ to minimize the error function

$$\Gamma = \frac{1}{N_{\text{train}}} \sum_{i=1}^{N_{\text{train}}} \left[(E_{\text{NN}}^i - E_{\text{DFT}}^i)^2 + \frac{\mu}{3N_{\text{atom}}^i} \sum_{j=1}^{3N_{\text{atom}}^i} (F_{j\text{NN}}^i - F_{j\text{DFT}}^i)^2 \right], \quad (2)$$

where N_{train} is the total number of training structures, N_{atom}^i is the number of atoms in structure i , μ controls the relative influence of the energies and the force components in the fitting, E_{NN}^i and E_{DFT}^i represent the NN and DFT total energies per atom, and $F_{j\text{NN}}^i$ and $F_{j\text{DFT}}^i$ are the NN and DFT force components. For the optimization of the NN potential the derivatives of this error function with respect to the weight parameters are calculated, and we note that individual atomic energies, which could be obtained from energy partitioning schemes, are not required.

First, a preliminary NN potential is generated from an initial reference data set, which is then further refined by including missing structures extracted from NN-based MD trajectories. Several procedures are available to identify relevant structures being still absent in the training set, which are described in detail elsewhere.^{99,100} Potentially critical structures are also identified by comparing the predictions of different NN potentials. This improvement of the potential by including more and more structures is performed iteratively until a converged NN PES has been obtained, which then allows to describe copper–water interfaces in the pressure and temperature range of interest.

A summary of the bulk water/ice, bulk copper/cuprous oxide and water–copper interface geometries in the final reference data set is given in the ESI,[†] Section 2. Additionally, interfacial

geometries with surface defects like adatoms, vacancies and steps, oxygen adatoms and Cu₂O adlayer are also included in the reference data set.

The NN MD simulations have been performed using the LAMMPS code¹²⁵ including a neural network extension for calculating the energies, forces and the stress tensor.¹²⁶ The copper–water interfaces are described by slab models, in which the vacuum region between the metal surfaces has been completely filled with water of an initial density of 1 g cm⁻³. The systems have then been equilibrated concerning pressure and temperature. For this purpose, *NPT* simulations employing a Nosé–Hoover thermostat and barostat^{127–130} at 300 K and 1 bar have been carried out for 1 ns with a time step of 0.5 fs yielding an equilibrium water density of about 0.91 g cm⁻³ far from the interface, which is consistent with previous results for pure RPBE-D3 bulk water.¹⁰⁴ In order to keep the positions of the copper atoms in the central layers of the slab bulk-like, which is required for a realistic model of a metal surface, the barostat has been coupled only to the dimension of the simulation box that is normal to the surface (Z in the present case). In all simulations of Cu(111) and Cu(100), the atoms of the two topmost metal layers at both surfaces are fully mobile, while the atoms of the central three layers have been frozen at the bulk positions. In case of Cu(110) the central four layers were kept fixed.

The production simulations have been carried out in the *NVT* ensemble for 1 ns at 300 K using the equilibrated lattice parameters obtained from the *NPT* simulations. Additionally, we have also performed and analysed *NVE* trajectories using uncorrelated snapshots from the *NVT* simulations as initial configurations, but we found that the corresponding results are essentially indistinguishable from the *NVT* data. Consequently, the following discussion regarding the copper–water interface simulations is restricted to the canonical ensemble.

4 Results

4.1 Construction of the neural network potential

The reference data set we have obtained in the self-consistent training process consists of the energies and force vectors of 10 293 structures containing up to 384 atoms as detailed in the ESI,[†] Section 2. About 10% of these structures (1035 energies and 161 213 force components) have been removed to be used for validation purposes in the test set. The remaining 9258 energies and 4 306 872 force components have been employed for training the NN potential.

The chemical environments of the Cu, O and H atoms, for which a cutoff radius of 12 Bohr has been found to be sufficient, are represented by 53, 53 and 51 symmetry functions, respectively, which serve as the input vectors for the atomic NNs. Several NN potentials with various numbers of neurons in the two hidden layers and different initial random weight parameters have been generated and optimized. Among the resulting NN potentials, the fit employing atomic NNs with 25 neurons per hidden layer exhibits the smallest energy and

Table 1 Root mean squared errors (RMSE) of the energies E_{RMSE} and forces F_{RMSE} in the training set. The values in parentheses represent the corresponding test set errors. The RMSEs are provided for all data in the respective sets as well as for several subgroups of different chemical composition. The number of structures corresponds to the number of energy values, while for each atomic environment three force components are available for training or validating the NN potential

Composition	Structures	Atomic environments	E_{RMSE} (meV per atom)	F_{RMSE} (meV per Bohr)
All data	9258 (1035)	1 435 624 (161 213)	0.8 (0.9)	66.5 (66.3)
Cu	489 (47)	8536 (664)	0.9 (1.2)	26.6 (27.9)
H ₂ O	6682 (766)	1 103 826 (126 690)	0.8 (0.8)	47.4 (46.9)
Cu + H ₂ O interface	1864 (195)	320 802 (33 487)	0.8 (1.4)	109.8 (113.2)
Cu ₂ O	223 (27)	2460 (372)	0.4 (0.4)	32.1 (36.2)

force RMSE values for the test set geometries and has been chosen for carrying out the simulations of the water–copper interface. The atomic NNs for copper and oxygen contain 2026 parameters each, while the number of weights for the atomic NN of hydrogen is 1976. Consequently, the NN potential in total includes 6028 fitting parameters, independent of the number of atoms in the system, since for a given element the parameters of the atomic NNs are the same. Therefore, there are about three orders of magnitude less fitting parameters than energies and force components in the training set that are used in their optimization. The RMSEs of the test set energies and forces are 0.9 meV per atom and 66.3 meV per Bohr, respectively, which is very close to the corresponding errors of the training set (0.8 meV per atom and 66.5 meV per Bohr), and consequently the energy and force predictions of the NN potential are in excellent agreement with DFT. In Table 1 the

fitting errors of the energies and force components for the entire training and test data sets as well as for subsystems of different chemical composition are compiled. Fig. 1(a) and (b) show histograms of the signed energy and force errors in the training set exhibiting the typical normal distributions centered at zero. The corresponding plots for the test set are given in panels (c) and (d). Further, Fig. 1 contains correlation plots of the NN and DFT energies and forces using different colors for the individual subsystems.

Apart from analysing the quality in the representation of the DFT energies and forces, we have further investigated the properties of the three constituent subsystems bulk copper, bulk cuprous oxide and bulk liquid water, as the correct description of these systems is mandatory for obtaining reliable results in the simulations of the interface. In Table 2 several properties of bulk copper and bulk cuprous oxide, *i.e.* the lattice

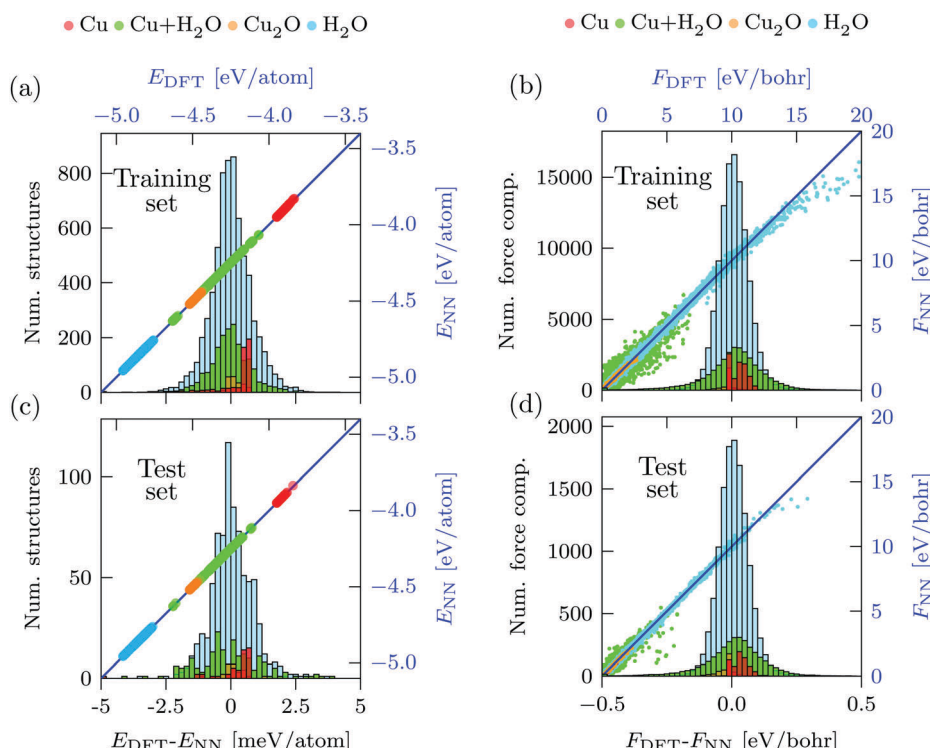


Fig. 1 Correlation plots of the NN and DFT energies (E_{NN} and E_{DFT}) of all structures in the training (a) and test set (c) (blue axis labels). Plots (b) and (d) show the correlation of the absolute values of the forces F_{NN} and F_{DFT} acting on atoms in the training and in the test set. Further, all panels contain the histograms of the corresponding fitting error distributions $E_{\text{DFT}} - E_{\text{NN}}$ or $F_{\text{DFT}} - F_{\text{NN}}$, respectively. In all histograms the numbers of structures for the H₂O and Cu + H₂O subsystems have been scaled by a factor of 10 for clarity.

Table 2 Properties of bulk copper, bulk cuprous oxide and hexagonal ice (I_h) as obtained from DFT, the NN potential and in experiment. For the DFT calculations, D3 corrections as obtained from the DFT-D3 code v3.1 rev 0 are added to the RPBE energies and forces obtained from VASP

Method	Lattice constant [Å]		Bulk modulus [GPa]		Cohesive energy		I_h lattice volume [Å ³ per H ₂ O]	I_h lattice energy [meV per H ₂ O]
	Cu	Cu ₂ O	Cu	Cu ₂ O	Cu [eV per atom]	Cu ₂ O [eV per Cu ₂ O]		
DFT	3.58	4.34	143.5	96.5	-3.70	-11.06	32.21	-610.2
NN	3.57	4.35	142.9	96.7	-3.70	-11.06	32.30	-610.3
Expt.	3.61 ¹³²	4.27 ¹³²	140.0 ¹³³	112.0 ¹³⁴	-3.51 ¹³⁵	-11.30 ¹³²	32.05 ¹³⁶	-609.6 ¹³⁷

Table 3 Properties of bulk liquid water calculated in NN-based MD simulations of systems containing 128 water molecules. All NN values for diffusion coefficient and hydrogen bond lifetime refer to the NVE simulations performed at NPT equilibrated density, 300 K and 1 bar. The NN_{interface} data has been obtained using the NN potential for the ternary Cu/O/H system developed in the present work, while the NN_{bulk} data has been determined using a NN potential constructed for pure water in a previous study.¹⁰⁴ The errors bars are obtained from the mean deviations of the respective quantities from 10 independent NVE trajectories. For comparison also the experimental values are given

Property	NN _{interface}	NN _{bulk}	Expt.
Equilibrium density [g cm ⁻³]	0.907	0.895	0.995 ¹³⁸
Diffusion coefficient [10 ⁻⁵ cm ² s ⁻¹]	2.23 (+0.29/-0.34)	2.25 (+0.35/-0.34)	2.31 ¹³⁹
Hydrogen bond lifetime [ps]	2.52 (+0.30/-0.15)	2.53 (+0.31/-0.15)	

constant, the bulk modulus and the cohesive energy along with the lattice energy and lattice volume of hexagonal ice as provided by DFT, the NN potential and experiment, are listed. We find that for all investigated properties the NN potential exhibits an excellent agreement with the underlying DFT data and also with experiment. In previous work¹⁰⁴ we have thoroughly investigated the description of water by NN potentials based on different exchange correlation functionals including the RPBE-D3 functional used in the present work and compared these results with experimental and theoretical data. In Table 3 the equilibrium density, the diffusion coefficient and the hydrogen-bond lifetimes of bulk water at 300 K have been compiled and compared to experiment as well as to the corresponding values obtained using a NN potential for pure liquid water developed in previous work.¹⁰⁴ Finally, the oxygen–oxygen radial distribution function at 300 K is shown in Fig. 2.

4.2 System size convergence

For a reliable determination of the properties of interfacial water, two requirements need to be met: sufficient sampling of

the configurations of the liquid water by long MD simulations and a converged system size. For the convergence tests regarding the size of the water region, 7 layer Cu(111) slabs have been used to test the supercell size and the water film diameter d , which is defined as the distance between the average positions of the copper atoms in the topmost layers of both surfaces. First, supercells ranging from (3 × 3) to (9 × 9) have been tested in combination with an approximately 40 Å water film. The compositions of these systems as well as the equilibrated water diameters d_{eq} are listed in Table 4. In a second step d has been tested in 5 Å steps from 10 to 40 Å using a (9 × 9) supercell. The corresponding systems are compiled in Table 5. The NPT equilibrated water film diameter deviates slightly from the target value depending on the number of inserted water molecules.

First, we have investigated the probability distribution of the oxygen atoms along the direction perpendicular to the surface to identify the required system size for obtaining a bulk-like water region in the center of the water film (see ESI,† Section 3 for the computation methodology). The corresponding oxygen density profiles, which have been normalized to the oxygen density in bulk liquid water, are plotted in Fig. 3. As expected, the oxygen density close to the surface strongly deviates from

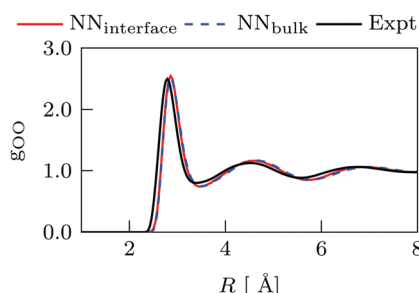


Fig. 2 Oxygen–oxygen radial distribution function (RDF) g_{OO} for bulk liquid water obtained from NN-based MD simulations at 300 K and the equilibrium density (see Table 3). The NN_{interface} RDF has been calculated using the NN potential for the ternary Cu/O/H system developed in the present work, while the NN_{bulk} RDF has been determined using a NN potential for pure bulk water constructed in a previous study.¹⁰⁴ For comparison, also the experimental data is given ref. 140.

Table 4 Number of water molecules $N(H_2O)$ and copper atoms $N(Cu)$ in the MD simulations of the water/Cu(111) interface represented by different supercells of a 7-layer metal slab. The water film diameters d_{ini} and d_{eq} refer to the distances between the copper atoms of the topmost metal layers before and after the NPT equilibration of the cell perpendicular to the surface, respectively. The variations in d_{eq} result from the different number of water molecules in the vacuum region for each supercell

Supercell	$N(H_2O)$	$N(Cu)$	d_{ini} [Å]	d_{eq} [Å]
(3 × 3)	62	63	40	44.1
(4 × 4)	111	112	40	43.6
(5 × 5)	164	175	40	41.6
(6 × 6)	238	252	40	41.4
(7 × 7)	324	343	40	41.7
(8 × 8)	395	448	40	39.1
(9 × 9)	528	567	40	41.1

Table 5 Number of water molecules $N(\text{H}_2\text{O})$ and copper atoms $N(\text{Cu})$ used in the convergence tests concerning the water film diameter d using a 7-layer (9×9) Cu(111) supercell. The values of d_{ini} and d_{eq} refer to the thickness before and after the *NPT* equilibration of the cell perpendicular to the surface, respectively. The deviations of d_{eq} from the initial value result from the inserted number of water molecules

$d_{\text{ini}} [\text{\AA}]$	$N(\text{H}_2\text{O})$	$N(\text{Cu})$	$d_{\text{eq}} [\text{\AA}]$
10	97	567	8.8
15	166	567	14.7
20	234	567	19.5
25	312	567	25.2
30	387	567	30.7
35	450	567	35.4
40	528	567	41.1

the bulk value and exhibits a pronounced structure, which decays into a bulk-like density region only for a water film diameter of at least 30 Å. For instance, the density of the water molecules immediately at the interface is much higher than that of the bulk region due to the formation of an ad-layer structure, which will be analyzed below. Further, three distinct hydration layers extending up to 10 Å on either side of the metal slab can be identified so that for a 40 Å water film, the two interfacial water regions are well separated by thick bulk water region spanning almost 20 Å along the surface normal.

The dependence of the oxygen probability density on the supercell size is less pronounced, but even in the 1 ns trajectories we have calculated there is still a notable noise level in the data for the smaller cells, which becomes negligible only

at a supercell size of approximately (6 × 6). This is likely a consequence of two effects, the improved statistics due to the larger number of molecules in the larger cells and the lower lateral correlation of the molecular motions in the more extended supercells. We note that for sufficiently large systems, the peak heights and positions close to the surface become completely independent of the size of the supercell and the water film diameter. Thus, in this case the small changes in the simulation cell dimension along surface normal, resulting for instance from the *NPT* equilibration of the system delivering slight variations depending on the initial number of water molecules, are fully accommodated by a corresponding change in the thickness of central bulk water-like region.

The coverage of the Cu(111) surface by water molecules in the first hydration layer is compared for different supercells and water films in Fig. 4 and demonstrates that the overall number of water molecules in the first hydration layer is less sensitive to the dimensions of the water region than the oxygen probability distribution along the surface normal discussed before. On average, there is approximately one water molecule per two surface copper atoms in the first layer. About 20–25% of these water molecules are located in the smaller first peak close to the surface, while the majority of water molecules resides in the substantially larger second peak.

Apart from the water structure close to the surface, another indicator for the system size convergence is the water region in the center of the water film, which should possess bulk-like properties to ensure that the water structures at both metal

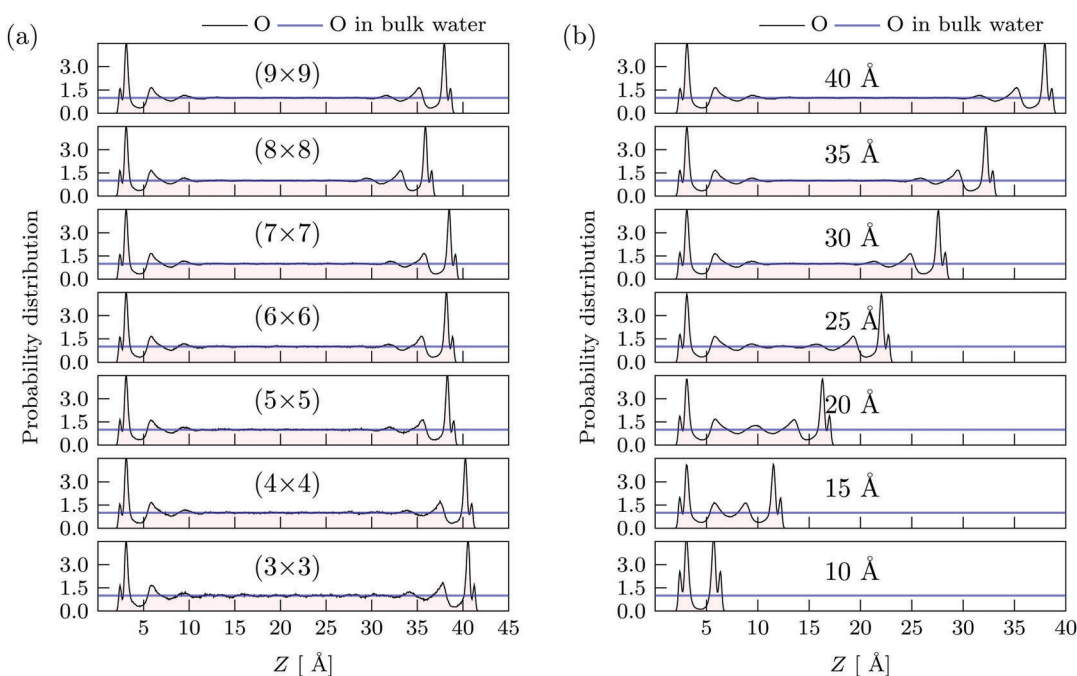


Fig. 3 (a) Probability distribution of the water oxygen atoms along the surface normal Z for different supercells of the Cu(111) surface and a 40 Å water film diameter. (b) Probability distribution of the water oxygen atoms along the surface normal of a (9 × 9) supercell of the Cu(111) surface for different water film diameters defined as the distance between the average Z coordinates of the topmost layer copper atoms. Due to the exclusion volume originating from the surface atoms and the equilibration of the system the effective water film diameters differ slightly from the indicated initial values. In all panels the blue line represents the average value in bulk water at 300 K, which has been set to one for normalizing the data.

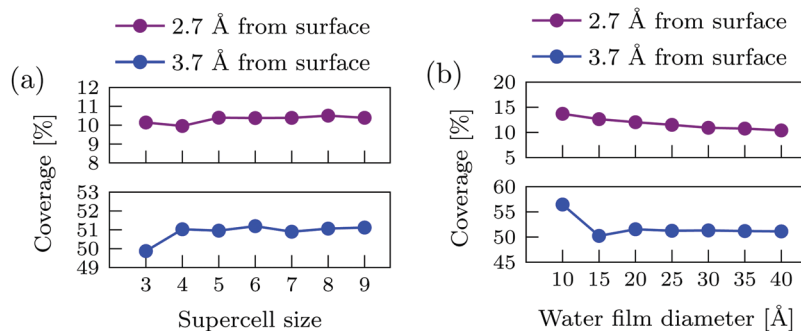


Fig. 4 Average coverage of the Cu(111) surface by water molecules in the first hydration layer up to the first (2.7 Å) and second peak (3.7 Å) in the oxygen probability density (cf. Fig. 3) for different supercells (a) and water film diameters (b). The axis label of the water film diameter refers to the initial interface before equilibration, the equilibrated values are listed in Table 5.

surfaces are fully decoupled. In Fig. 5 and 6 the oxygen–oxygen radial distribution functions (RDFs) for the water molecules within 1 Å from the center of the water film are plotted for different water film diameters and supercells, respectively (see ESI,† Section 4 for the computation methodology). Further, the difference plots of the RDFs $\delta(g_{\text{OO}})$ and the integrated RDFs (coordination number) $\delta(\int g_{\text{OO}})$ of the selected water molecules with respect to the RDF of bulk liquid water are shown. From Fig. 5 it is evident that even for a water film diameter of 30 Å there are still notable differences to bulk water, while an extremely small deviation is obtained for $d = 40$ Å. This is to be expected because the oxygen–oxygen RDF of bulk water shows features up to about 10 Å, or a sphere of 20 Å diameter, which is only unaffected by the presence of the surface, if there

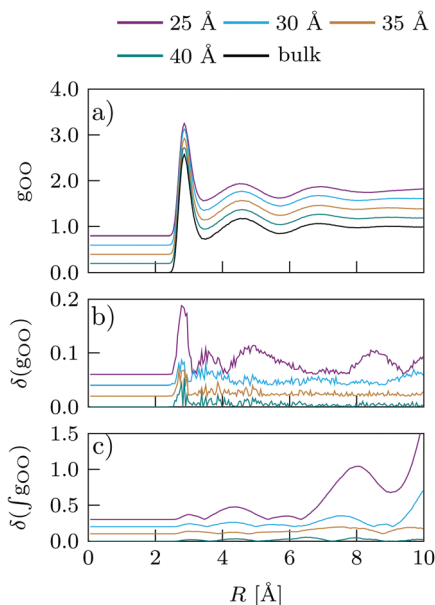


Fig. 5 (a) Oxygen–oxygen radial distribution functions (RDF) g_{OO} calculated in a (9×9) Cu(111) supercell with different water film diameters. The data sets are plotted with offsets for clarity. For each water film diameter the deviation $\delta(g_{\text{OO}})$ from the bulk water RDF is given in (b) and the deviation of the integral RDFs $\delta(\int g_{\text{OO}})$ in (c). The RDFs have been determined taking only the environments of the oxygen atoms within 1 Å from the centre of the water film into account.

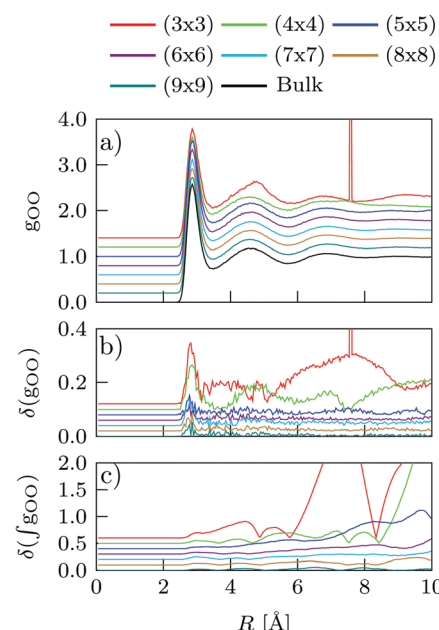


Fig. 6 (a) Oxygen–oxygen radial distribution functions (RDF) g_{OO} in the bulk region for different supercells using a water film diameter of about $d = 40$ Å. The RDFs have been determined taking only the environments of the oxygen atoms within 1 Å from the centre of the water film into account. For comparison also the RDF of bulk liquid water is shown (black line). The data sets have been shifted for clarity. In the (3×3) cell, the peak at about 7.5 Å is an artifact due to the periodic boundary conditions and results from the images of the central atom. The deviation $\delta(g_{\text{OO}})$ and the integral RDFs $\delta(\int g_{\text{OO}})$ from the bulk water RDF is provided in (b) and (c), respectively.

is no overlap with the modified water structure resulting from the surface. Also concerning the supercell size, the RDFs in Fig. 6 proves to be a more sensitive property than the oxygen probability distribution perpendicular to the surface in Fig. 3. A fully satisfying agreement with bulk water is only achieved for (8×8) supercells, which have a lateral distance of approximately 20 Å between the periodic images of the atoms.

Apart from these static structural properties of the interfacial and the bulk-like water regions, also dynamical properties like hydrogen bond lifetimes need to be tested for convergence. They can be calculated, e.g., from the hydrogen bond time

correlation function using the stable state picture (SSP) approach.¹³¹ In the stable state picture definition, we find the time taken for the “reactant” configuration, in this case a hydrogen bond $O_d-H_d\cdots O_a^x$ where O_d and H_d belong to the donor molecule and O_a^x is the acceptor oxygen in molecule x at $t = 0$ to leave its potential well resulting in a product configuration $O_d-H_d\cdots O_a^y$. In the literature, two main classes of hydrogen bond definitions are commonly used, one based on an energy criterion and the other on geometric considerations. In the present work we generally employ a geometric definition in which a hydrogen bond exists if the distance between the donor oxygen (O_d) and acceptor oxygen (O_a), R_{OO} , is less than 3.5 Å and the angle $\angle HOO$ is smaller than 30° (see Fig. 7). Specifically for the purpose of the lifetime calculation using SSP, a tighter hydrogen bond criterion ($R_{OO} < 3.2$ Å and $\angle HOO < 20^\circ$) is needed in order to define the stable state of the reactant hydrogen bond. Only those hydrogen bonds that satisfy this stricter criterion in the correlation time origin (reactant) are considered for the life time calculation. The hydrogen bond is considered to be broken when its R_{OO} gets larger than 3.8 Å or when its $\angle HOO$ gets larger than 40° or if a new acceptor oxygen atom fulfils the criterion. This definition is advantageous since it eliminates the overestimation due to recrossing events and settling time of the hydrogen bond in the product well.

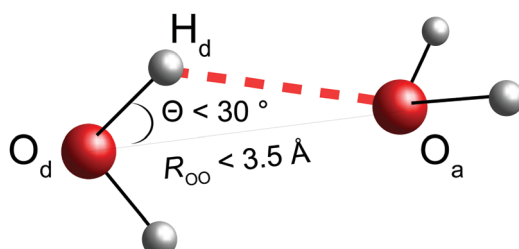


Fig. 7 Geometric hydrogen bond definition used in the present work. The subscripts “a” and “d” label atoms of the acceptor and donor molecules, respectively.

The hydrogen bond time correlation function is defined as

$$c_{HB}(t) = \frac{\langle h(0)a(0)h(t) \rangle}{\langle h(0) \rangle}, \quad (3)$$

where the operator $h(t)$ is one if the reactant hydrogen bond that was present at time $t = 0$ keeps existing without interruption until time t , and 0 otherwise. $a(0)$ will be one if the hydrogen bond at the time origin of the time correlation is located within the selected region of the simulation cell (interfacial region or bulk region) and 0 otherwise. The auto-correlation function is obtained by following the hydrogen bonds that are initially present within the selected region for 20 ps even if they leave this region within that time period. The resulting function $c_{HB}(t)$ is then fitted to an exponential form $\exp(-t/\tau)$, where τ is the hydrogen bond lifetime. We have computed the hydrogen bond lifetimes of the interfacial water molecules within 5 Å from the surface and in the bulk water region within 2.5 Å from the centre of water film. The results are shown in Fig. 8(a) and (b) for different supercells and water film diameters, respectively. From Fig. 8(a) it is evident that the average hydrogen bond lifetime in the interfacial region for Cu(111)/H₂O interface is lower compared to that of bulk region. In other words, the hydrogen bond dynamics is faster in the interfacial region when compared to the bulk region. The hydrogen bond lifetimes for bulk and interfacial water in the (3 × 3) supercell are clearly too high indicating that this small system size induces an artificial stabilization of the hydrogen bond network. In Fig. 8(b) the lifetimes in the “bulk region” for a water film diameter $d < 25$ Å are given only for reference as the sampled region does not exhibit any bulk water-like region and a clear convergence can only be observed for $d > 30$ Å.

Further, the residence lifetime of the water molecules at the copper surface has been analysed in a similar way using the correlation function

$$c_{residence}(t) = \frac{\langle a(0)a(t) \rangle}{\langle a(0) \rangle}. \quad (4)$$

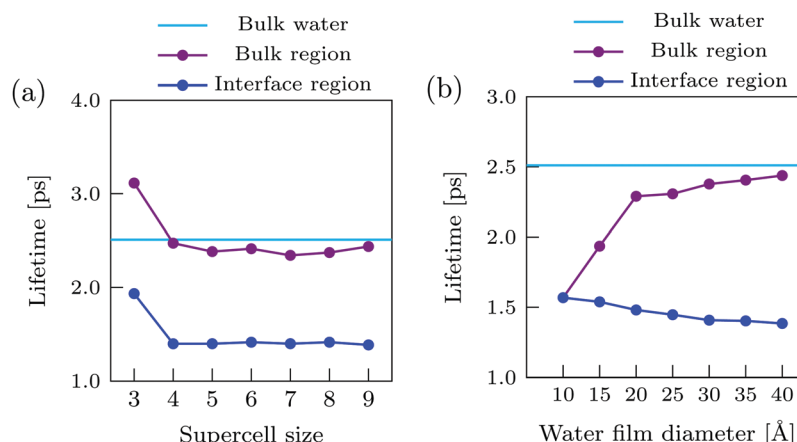


Fig. 8 Hydrogen bond lifetimes based on the stable state picture (SSP)¹³¹ lifetime definition in the bulk region and in the interfacial region at Cu(111) (up to 5.0 Å from the surface) for different supercells using a water film diameter of approximately 40 Å (a), and for different water film diameters employing a (9 × 9) supercell (b). The lifetime values have been obtained from an exponential fit of the hydrogen bond time correlation function. The straight line at 2.5 Å corresponds to the hydrogen bond lifetime in pure bulk water.

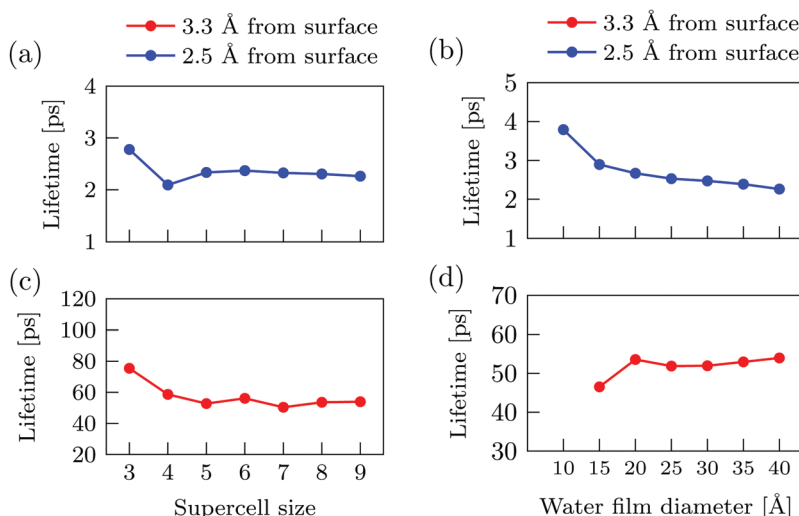


Fig. 9 Lifetimes of the water molecules in the first peak region up to 2.5 Å of the first hydration layer (see Table 10) and in full first hydration layer (up to 3.3 Å above the surface) at Cu(111) computed within the SSP lifetime definition for different supercells and a water film diameter of approximately $d = 40$ Å ((a) and (c)) and for a (9×9) supercell with different water film diameters ((b) and (d)).

Like for the hydrogen bonds we have used two criteria, a strict one (“well”) for selecting the molecules to be considered in the residence time correlation function and a loose one to check if the molecules have crossed the “barrier”, *i.e.* if they left the surface region. Here, $a(t)$ is 1 if the water molecule does not cross the “barrier” until time t . $a(0)$ is 1 if the water molecule

fulfills the strict criterion (residing within the “well”) at $t = 0$. The resulting time correlation function is fitted to an exponential function similar to the hydrogen bond lifetime discussed above. According to Fig. 9(a) the water molecules very close to the surface (2.54 Å from the surface) in a (3×3) supercell (barrier at 2.88 Å from the surface) reside longer compared to the larger supercells. We speculate that this phenomenon is similar to the diffusion process of an atom in a close packed bulk metal, which has a lower barrier in larger supercells due to the higher structural flexibility. Fig. 9(b) shows the convergence behavior of the residence lifetime with increasing water film diameter. In general the lifetime decreases with increasing separation between the surfaces. The lifetime of the water molecules within the complete first hydration layer (3.33 Å from the surface and barrier at 5.40 Å from the surface) is

Table 6 Number of water molecules $N(\text{H}_2\text{O})$ and copper atoms $N(\text{Cu})$ used in the MD simulations of the different interfaces. A water film thickness of approximately 40 Å has been employed in all cases

Surface	$N(\text{H}_2\text{O})$	$N(\text{Cu})$	Cu layers	Supercell
Cu(111)	719	700	7	$(10,0) \times (-5,10)$
Cu(100)	566	504	7	(6×6)
Cu(110)	490	576	12	(8×6)

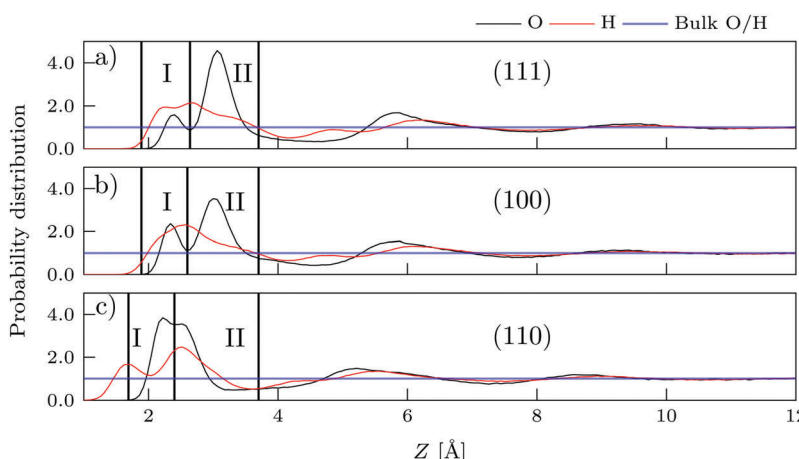


Fig. 10 Probability distribution of the oxygen (black) and hydrogen (red) atoms in the interfacial water region along the surface normal Z for the Cu(111)-, Cu(100)- and Cu(110)-surfaces using a 40 Å water film at 300 K. The data for both elements has been normalized to the corresponding distributions in bulk water (blue line). $Z = 0$ corresponds to the average position of the surface copper atoms in the topmost layer. The Z values defining regions I and II are given in Table 7.

shown in Fig. 9(c) and (d). The observations are essentially the same as for the first peak region only, with the interesting exception of a 15 Å water film diameter in (d), which might be an artifact of the very small system.

4.3 Interfacial water at low index copper surfaces

For the investigation of the properties of interfacial water at the low-index Cu(111), Cu(100), Cu(110) surfaces MD simulations at 300 K have been carried out for 1 ns. Based on the system size convergence tests in the previous section, which demonstrate that different properties of the system show different convergence characteristics, we have decided to employ large systems. For the Cu(111) surface, a $(10,0) \times (-5,10)$ supercell containing 7 copper layers has been used. The definition of this supercell is detailed in ESI,[†] Section 5. The Cu(100) and Cu(110) surfaces

have been represented by a (6×6) supercell with 7 copper layers, and a (8×6) supercell with 12 layers, respectively. In all cases a water film diameter of about 40 Å has been selected. The total number of water molecules and copper atoms in these simulations are compiled in Table 6. For Cu(111) and Cu(100), the three central metal layers have been frozen, while for Cu(110) four layers in the middle of the slab have been constrained at the bulk positions.

First, the bulk normalized distribution of the oxygen and hydrogen atoms in the interfacial region along the direction perpendicular to surface has been computed for all surfaces as shown in Fig. 10. Three distinct hydration layers are visible from the oxygen distribution in all cases extending up to 10 Å from the surface. In particular the shape of the first hydration layer located within 4 Å from the surfaces is very different for

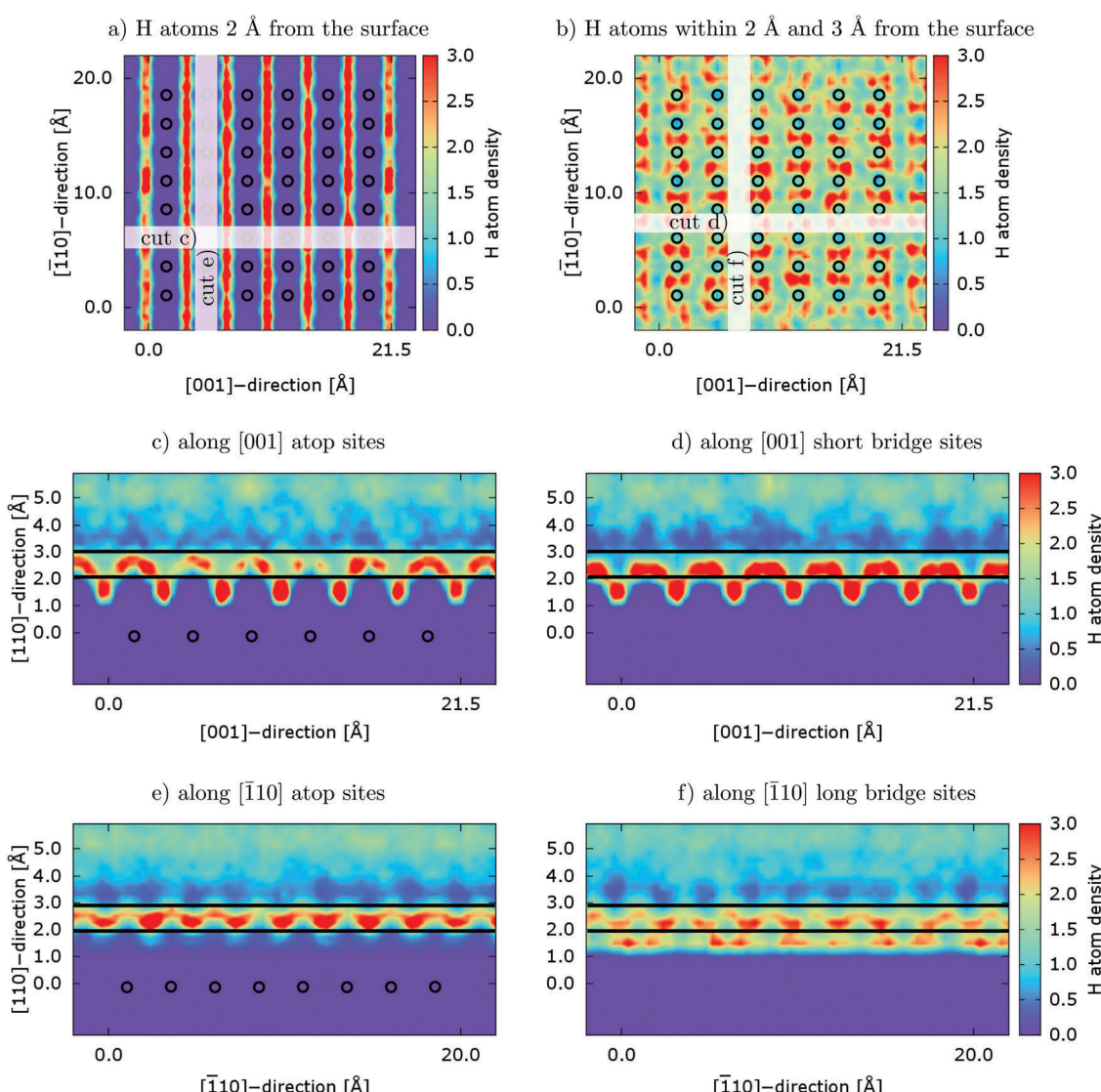


Fig. 11 Top views of the density of the hydrogen atoms within 2 Å (a) and between 2 and 3 Å from the Cu(110) surface (b) are shown. The positions of the topmost copper layer atoms are indicated as black circles. Panels (c–f) contain the hydrogen atom densities in slices perpendicular to the surface as indicated in panels (a and b). Close to the surface, the hydrogen atoms are localized in the valley region between the close packed copper atom rows, which gives rise to the first peak of the H distribution in Fig. 10c. For the larger distance shown in (b) most H atoms are in the short bridge sites.

each interface. In general, it exhibits a double peak structure and the first peak is notably smaller compared to the second peak except for the case of Cu(110), for which both peaks almost merge and appear closer to the surface. Concerning the oxygen atoms, the second and third hydrations layers are less pronounced and do not show any substructure. Overall, they are very similar for Cu(111) and Cu(100), while for Cu(110) the peaks of the second and third hydration layers are slightly closer to the surface. This is a consequence of the more open structure of Cu(110), which enables a closer approach of the water molecules to the surface in the valley in between the topmost copper rows. This can be seen in Fig. 11, in which the hydrogen atom density at the Cu(110) surface is plotted for all hydrogen atoms within 2 Å from the surface in panel (a) and between 2 and 3 Å from the surface in panel (b). Close to the surface, there is a high probability to find hydrogen atoms in the valleys, which is also evident from the cuts along the surface normal in Fig. 11(c) and (d). At a distance between 2 and 3 Å from the surface the highest probability for the hydrogen atoms is close to the short bridge sites (panel (e)). A discussion of the corresponding oxygen atom probability density and the molecular orientations in provided further below.

In Fig. 12, the distribution of all hydrogen atoms and of those not involved in forming hydrogen bonds are shown for the three interfaces. In bulk water simulations at 300 K using the same potential, on average about 87.5% of the hydrogen atoms participate in hydrogen bonding, and this value is reached far from the surface at all interfaces. On the other hand, most hydrogen atoms very close to the surface and a small fraction of hydrogen atoms located approximately around 5 Å (4 Å in case of Cu(110)) do not participate in hydrogen bonding, which is common for all interfaces. To understand these observations, we have investigated the distribution of the oxygen–oxygen distances $R_{O_dO_a}$ in the hydrogen bonds (Fig. 13)

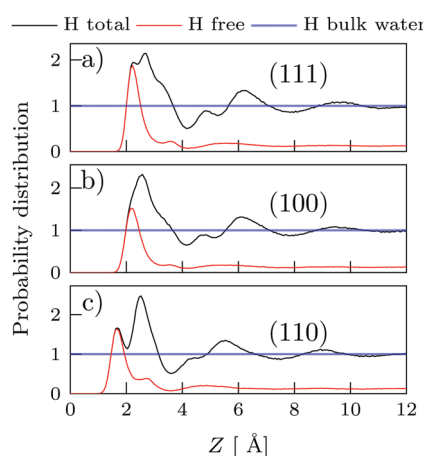


Fig. 12 Probability distribution of all hydrogen atoms (black lines) and the hydrogen atoms not participating in hydrogen bonds (red lines) along the surface normal for the Cu(111)-, Cu(100)- and Cu(110)-surfaces obtained for a water film thickness of 40 Å at 300 K. The curves have been normalized to the density in bulk water (blue line). Far from the surface 87.5% of the hydrogen atoms participate in hydrogen bonds, which corresponds to the fraction in bulk liquid water.

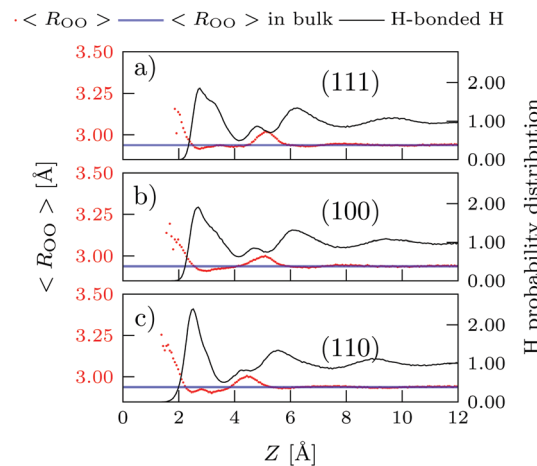


Fig. 13 Average oxygen–oxygen distances $\langle R_{OO} \rangle$ between hydrogen-bonded water molecules along the surface normal Z for the Cu(111)-, Cu(100)- and Cu(110)-surfaces (red). The assignment of the distances to Z values has been based on the position of the shared hydrogen atom in the hydrogen bonds. The blue line corresponds to the average oxygen–oxygen distance of hydrogen-bonded molecules in bulk liquid water simulations using the same NN potential (2.94 Å). For reference, the probability distribution of the hydrogen-bonded H-atoms is plotted as black line showing that the strongly extended values of $\langle R_{OO} \rangle$ for $Z < 2$ Å originate from a very small number of hydrogen bonds.

and the HO_dO_a angles (Fig. 14) as a function of the distance from the surface. The relatively few hydrogen bonds formed within 2.5 Å from the surface have longer bond ($\langle R_{OO} \rangle$) distances compared to that of those in the bulk region (see Fig. 13) and an extended hydrogen bond angle (Fig. 14). This indicates that the formation of typical hydrogen bond geometries is hindered by the presence of the surface, which also reflects in the small fraction of hydrogen bonds. The peak at around 5 Å (4 Å in the case of Cu(110)) is mostly populated by hydrogen atoms that bridge the water molecules in the first and second

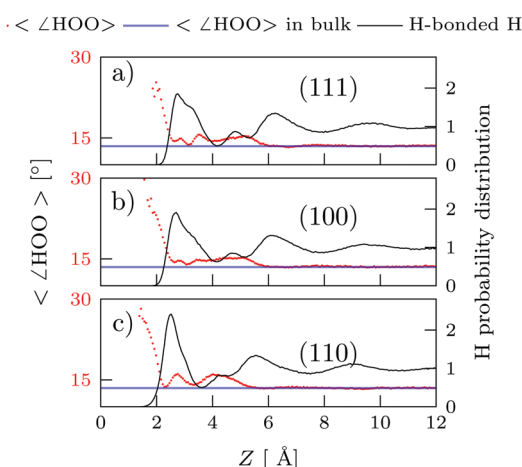


Fig. 14 Average distribution of HO_dO_a bond angles as defined in Fig. 7 as a function of the distance from the surface Z for the Cu(111)-, Cu(100)- and Cu(110)-surfaces. The blue line corresponds to the average hydrogen bond angle in bulk water simulations (13.47°). The probability density of the hydrogen bonded hydrogen atoms is shown in black for reference.

hydration layers. The hydrogen bonds in this region are also slightly longer than those in the bulk region and have larger HO_dO_a angles.

For a detailed analysis of the water density distribution, the first hydration layer of the interfaces has been split into two regions, a first peak region I and a second peak region II as labeled in Fig. 10. The exact location of these regions at the different interfaces is listed in Table 7. The average density profiles of the oxygen atoms are shown in Fig. 15 for Cu(111) and Cu(100), and in Fig. 16 for Cu(110). The densities have been normalized to the density in the center of the water film, which is indistinguishable from the density in bulk liquid water, as is demonstrated in Fig. 17 for the example of the Cu(111) interface. This result is similar and to some extent

Table 7 Definition of the two peak regions shown in Fig. 10 for the three interfaces. The values of 'start' and 'end' denote the vertical distances from averaged positions of the surface copper atoms in the first layer

Region	(111)		(100)		(110)	
	I	II	I	II	I	II
Start [Å]	1.88	2.66	1.86	2.60	1.56	2.40
End [Å]	2.66	3.70	2.60	3.70	2.40	3.70

redundant to the density profiles in Fig. 3 and 10 in the middle of the water film, however in this figure the density has not been integrated over the directions parallel to the surface and thus shows small statistical density fluctuations due to the finite sampling time. In the contour plots, the average position of the surface copper atoms are represented by black circles. We find that the high oxygen atom densities in region I are localized at the atop metal sites for all the interfaces. In case of the Cu(110) interface, the long bridge sites are also populated, albeit on average at a slightly larger surface separation (cf. Fig. 16(c)). This observation is comparable with the one dimensional water chains observed by other researchers at the Cu(110) surface.^{21,77,78} The oxygen atoms in region II of the Cu(111) surface have no specific site preference, whereas at the Cu(100) interface the bridge sites and hollow sites exhibit a higher oxygen density compared to atop sites. In case of the Cu(110) interface (Fig. 16), a high density of oxygen atoms in region II is observed along the valley region between the close packed metal rows, while the short bridge sites in the (110) interface are not populated. From the density plots, we conclude that the level of ordering of the water molecules at the interfaces increase qualitatively from Cu(111) via Cu(100) to the Cu(110) surface. For a more quantitative analysis, we calculated

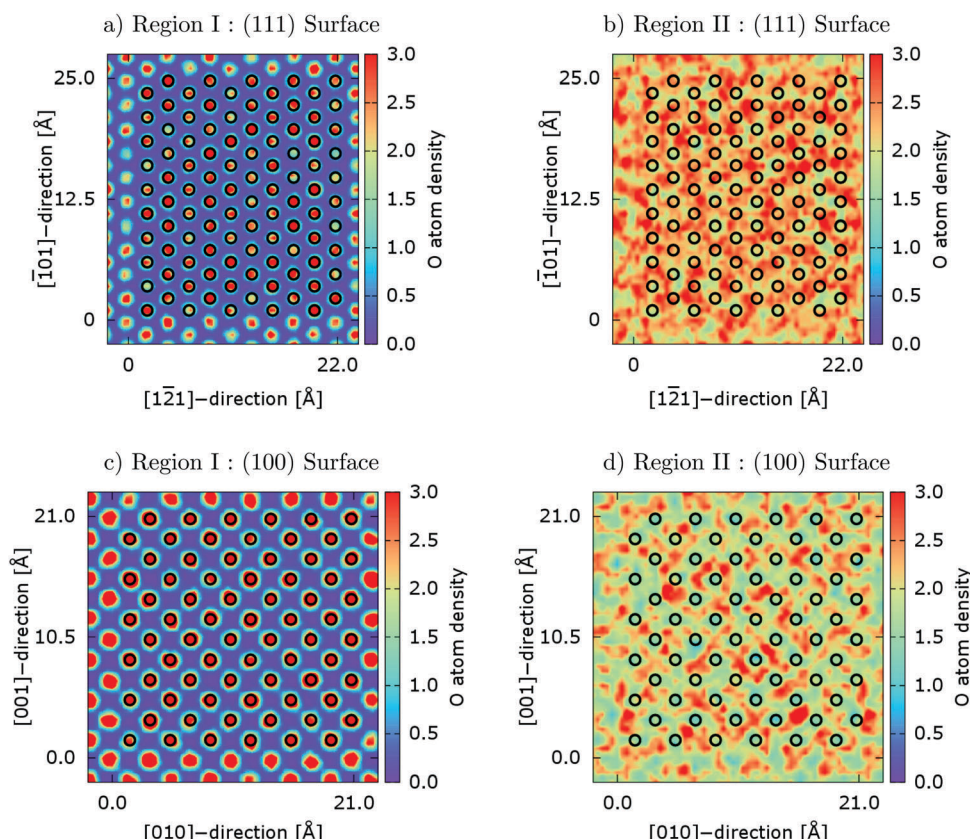


Fig. 15 Contour plots showing the probability distributions of the oxygen atoms in first (I) and second (II) peak region of the first hydration layer at the Cu(111) and Cu(100) surfaces. The black circles represent the average position of the topmost layer copper atoms. For both surfaces, a high oxygen density in the atop position is observed in region I. The oxygen atoms in region II do not exhibit a pronounced structure at the Cu(111) surface, while there is a higher probability for bridge and hollow sites at the Cu(100) surface. The values are normalized to the density of oxygen atoms in liquid bulk water simulation (O atom density = 1.0).

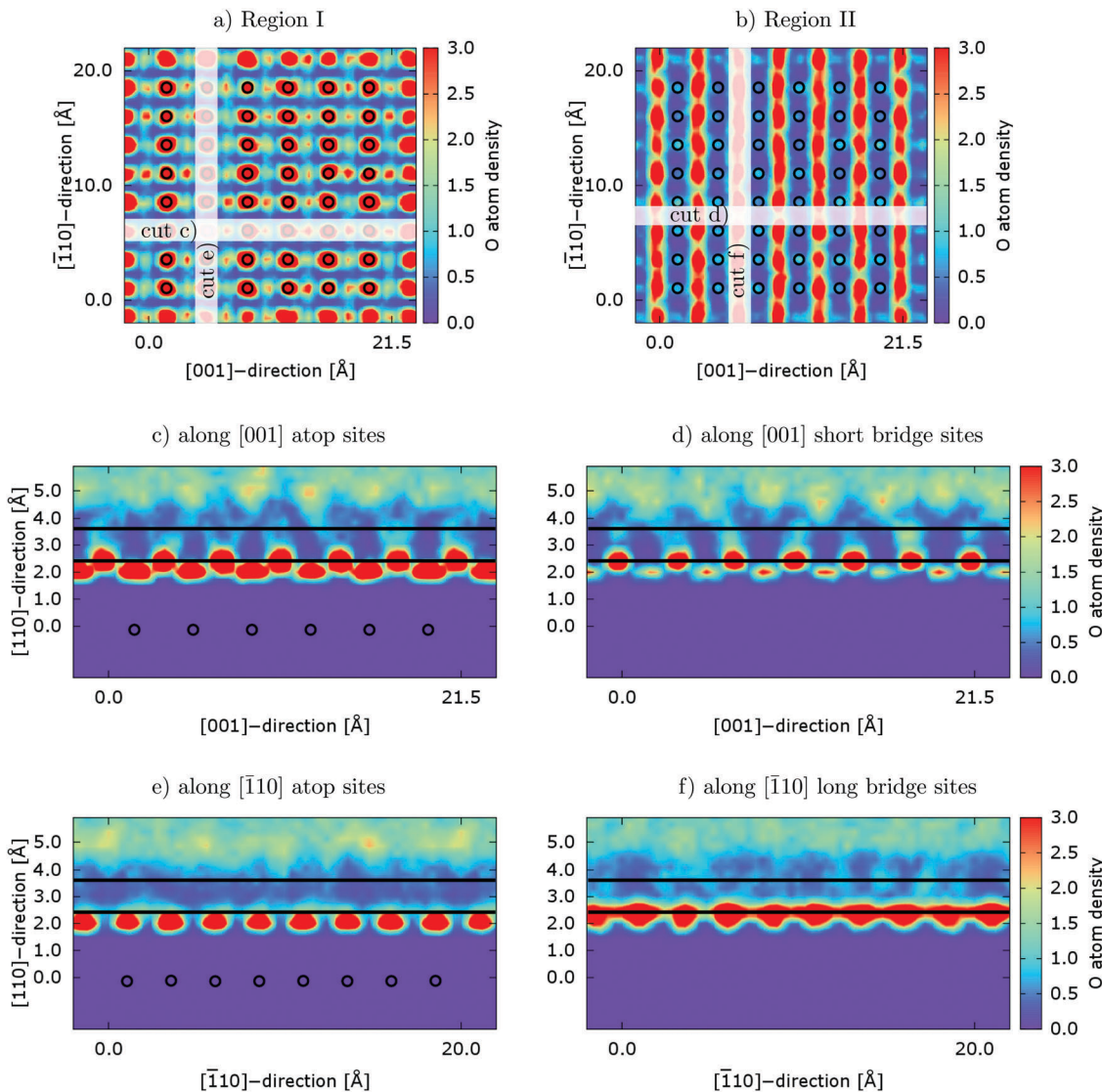


Fig. 16 Top views showing the distribution of oxygen atoms in the peak region I (a) ($1.56 < Z < 2.40 \text{ \AA}$) and peak region II (b) ($2.40 < Z < 3.70 \text{ \AA}$) of the first hydration layer at the Cu(110) surface. The black circles represent the average positions of the top layer copper atoms. In region I, a high oxygen density is present on top of the first layer copper atoms, whereas in region II, the oxygen atoms are predominantly located at long bridge sites. The values have been normalised to the corresponding density of oxygen atoms in bulk liquid water (oxygen atom density 1.0). Panels (c–f) contain the oxygen atom densities in slices perpendicular to the surface as indicated in panels (a) and (b).

the coverages by water molecules in regions I and II (see Fig. 18(a)). There is a very high coverage of 39% in case of the open Cu(110) surface in region I, while lower coverages of 17% for Cu(100) and 10% for Cu(111) have been found. Since we are comparing surfaces with different surface atom densities, the average number of water molecules per unit volume in region I and II of these interfaces are compared in Fig. 18(b). In region I, the average number of water molecules increases from Cu(111) via Cu(100) to the Cu(110), whereas, the opposite trend is observed for region II.

In addition to the probability density of the oxygen atoms, we have further analysed also the angular orientation of the water molecules in regions I and II at the different interfaces. For this purpose we have used three angles, an atop angle α , a dipole angle β and an OH angle γ with the surface normal as

defined in Fig. 19. The atop angle is the angle formed by the vector connecting each oxygen atom to its nearest Cu atom and the surface normal. The dipole angle and OH angle refer to the angle between the dipole vector or the OH bond vector with respect to the surface normal. The angles $\gamma_{\text{OH}1}$ and $\gamma_{\text{OH}2}$ refer to the shorter and longer OH bond of the water molecules, respectively. A summary of the average values of the above mentioned angles made by the water molecules in region I and II is given in Table 8. Fig. 20 and 21 show the correlations between these angles for all three interfaces in regions I and II, respectively. The water molecules in region I of the Cu(111) and Cu(100) interfaces prefer to stay at the atop metal position, which is evident from the maximum between 0° and 20° for α . The dipole vectors of these water molecules predominantly point away from the surface ($\beta < 90^\circ$). Since a majority of the

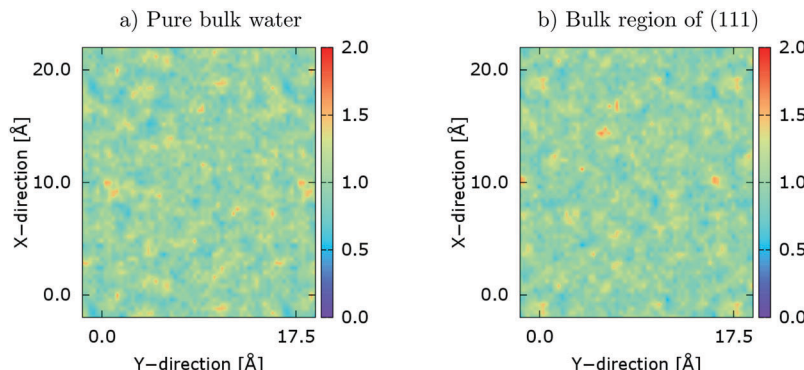


Fig. 17 Distribution of the oxygen atoms in a simulation of bulk water without a copper surface (a) and in the bulk region of the Cu(111)–H₂O interface system (b). Both simulations have been carried out in the same (8,0) × (−4,8) cell.

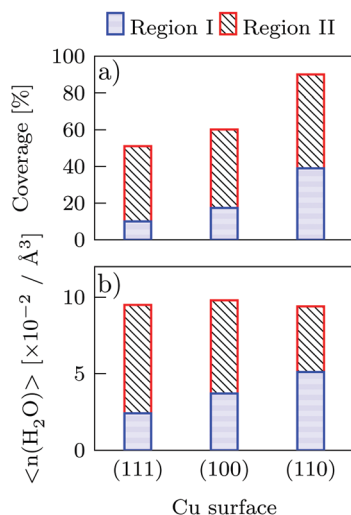


Fig. 18 Water coverage of the copper surfaces in the first hydration layer is given in panel (a) and the average number of water molecules per Å³ is provided in panel (b). The blue bars correspond to the first peak and the red bars to the second peak (see Fig. 10). Please note that Cu(110) is an open surface and the surface metal atom density is lower than the other two surfaces.

OH bonds prefers to align within 60° and 90° from the surface normal, we can conclude that on average the plane of the water molecule lies almost parallel to the surface with a maximum tilt of about 30° away from the surface.

In the region I of the Cu(110) interface, apart from a majority of oxygen atoms preferring atop sites, there are few oxygen

Table 8 Average values of the atop angle $\langle\alpha\rangle$, the dipole angle $\langle\beta\rangle$ and of the OH angles $\langle\gamma(OH1)\rangle$ and $\langle\gamma(OH2)\rangle$ of the water molecules in regions I and II at all interfaces. All angles, which are defined in Fig. 19, are given in degrees. OH1 and OH2 refer to the shorter and longer OH bond in the molecule, respectively

Surface	Region I			Region II				
	$\langle\alpha\rangle$	$\langle\beta\rangle$	$\langle\gamma(OH1)\rangle$	$\langle\gamma(OH2)\rangle$	$\langle\alpha\rangle$	$\langle\beta\rangle$	$\langle\gamma(OH1)\rangle$	$\langle\gamma(OH2)\rangle$
Cu(111)	12.9	58.8	72.0	72.7	16.7	118.1	105.6	112.4
Cu(100)	14.3	62.1	73.7	73.6	18.7	113.2	103.7	107.2
Cu(110)	22.5	75.6	75.3	81.3	28.7	117.0	102.2	116.2

atoms at the long bridge sites as seen in the density plots ($\alpha = 40^\circ$). While most of the water molecules at the atop sites have similar dipole and OH bond orientations as those at the Cu(111) and Cu(100) surfaces, a small fraction also has dipole vectors and OH bonds pointing towards the surface (around 140° for dipole angle and around 160° for OH angle). The few water molecules at the long bridge site behave similarly to the water molecules at the atop site with a majority of them having a dipole vector pointing away from the surface and OH bonds being almost parallel to the surface. There is no differentiation between the two OH bonds of the water molecules in region I at all the investigated interfaces. The average structure of water molecules in region I is comparable with the well established equilibrium geometry of the water monomer on copper surfaces.^{58,66}

The water molecules in region II of the first hydration layer at the Cu(111) interface exhibit an atop angle distribution between 0° and 30°, which due to the larger separation of this

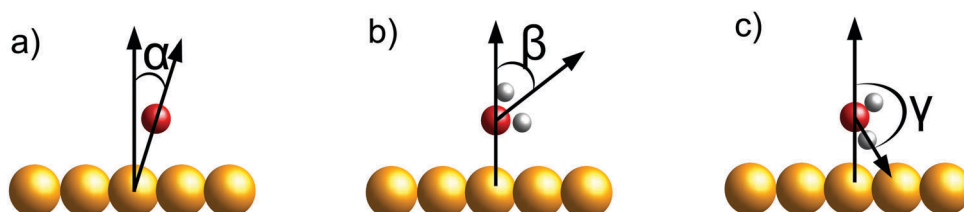


Fig. 19 Definitions of the angles plotted in Fig. 20 and 21. The atop angle α is the angle between the surface normal and the connection between the oxygen atom and the closest copper atom, the dipole angle β is the angle between the dipole vector and the surface normal, and the OH angle γ is the angle between an OH-bond in the water molecule and the surface normal.

Region I

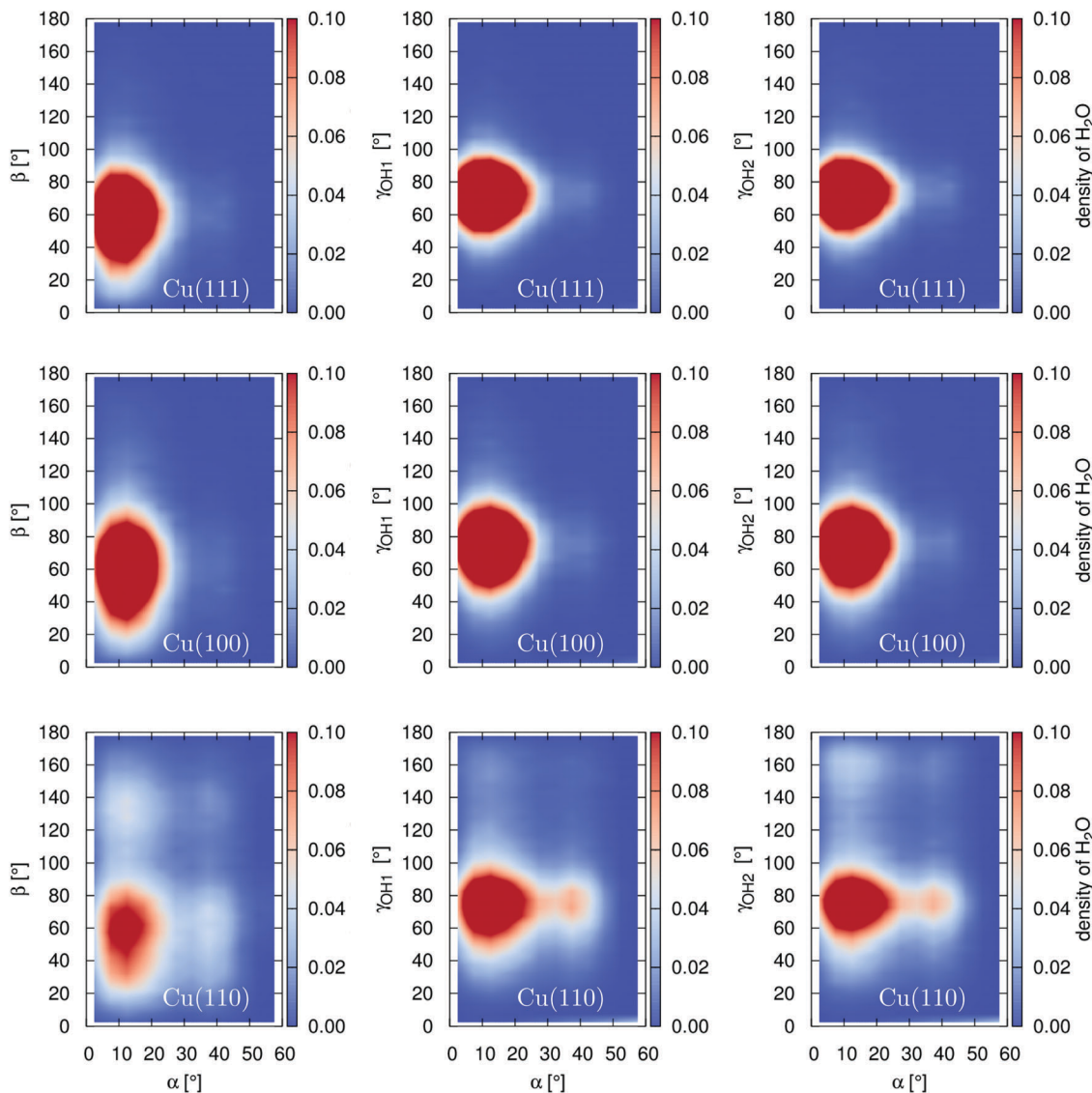


Fig. 20 Contour plots showing the correlations between the atop angle, dipole orientation angle and OH bond orientation angles of water molecules in region I of different surfaces. Atop angle is the angle between the vector connecting O atom of the water molecules in the first hydration layer with its nearest surface copper atom and the surface normal. The zero of atop angle is when the O atom of the water molecule sits exactly at the atop site. Dipole angle is the angle made by the dipole vector of water molecules in the first hydration layer with respect to the surface normal. The zero of dipole angle is when the dipole aligns with the surface normal while pointing away from the surface, 180 mark is when the dipole vector is pointing at the surface and 90 is when the dipole vector lies parallel to the surface. OH angle is the angle made by the OH bonds with the surface normal. The plotted angles are defined in Fig. 19.

region from the surface corresponds to atop as well as to higher coordination sites. In case of the Cu(100) interface, the maximum of the atop angle distribution is shifted towards slightly larger values indicating a preference for high coordination sites. At both surfaces, the dipole vector orientation is opposite to that of the region I, as the majority of water molecules in region II shows dipole vectors pointing towards the surface ($\beta > 90^\circ$). Moreover, there is a double maximum distribution for the OH bond orientations, one around 90° and the other around 155° . So, on average one of the OH bonds is aligned

parallel to the surface while the other is pointing towards the surface. For the Cu(110) interface, there is a strong preference of the water molecules in region II towards the high coordination sites (between 20° and 40°) as could be observed also in the corresponding density plots. Also here, the dipole angle is pointing towards the surface ($\beta > 100^\circ$) and the OH bonds are aligned similarly to the other interfaces.

In summary, we found that a majority of the water molecules in region I prefer position atop the metal sites and have their molecular plane nearly parallel to the surface with the oxygen

Region II

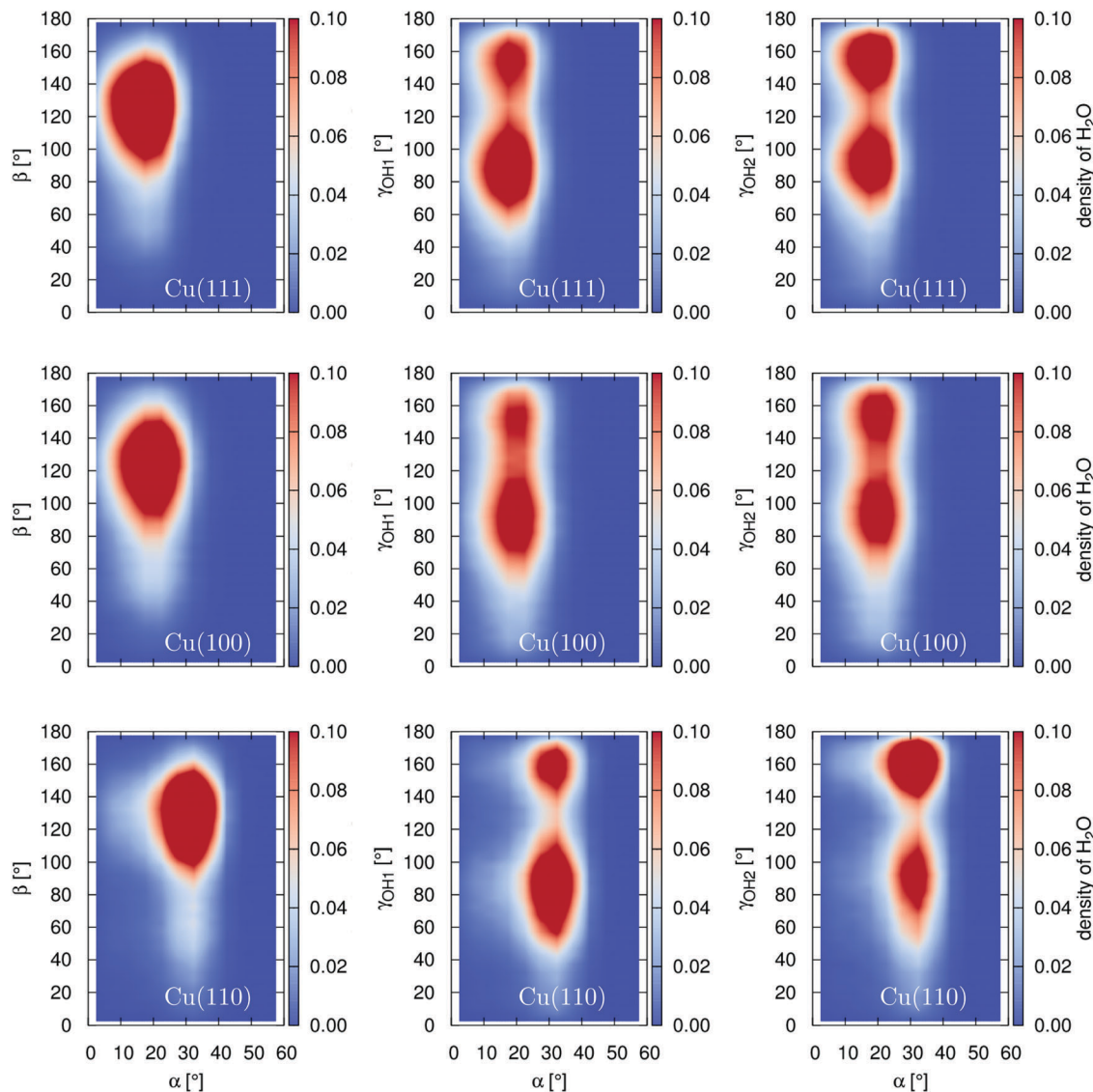


Fig. 21 Contour plots showing the correlations between the atop angle, dipole orientation angle and OH bond orientation angles of water molecules in region II of different surfaces are plotted. The plotted angles are defined in Fig. 19.

pointing slightly towards the surface while those in region II have predominantly “H-down” configurations.

Concerning the dynamical properties, the mean squared displacements (MSD) of the water molecules parallel to the surface are compared in Fig. 22 for the interfacial as well as for the bulk region. For the MSD calculation, all water molecules within 5 Å from the surface (in case of interfacial water) and within 2.5 Å from the centre of the water film (for bulk water) at $t = 0$ have been chosen. The water molecules are allowed to leave this region and their MSD is computed and averaged for 5 ps to prevent exchanges of water molecules between the bulk and interfacial regions. From Table 9, we see that as expected the diffusion coefficients (D_{xx} and D_{yy}) of the bulk water molecules are very similar for all interfaces. For the interfacial water, on the other hand, the diffusion coefficients decrease in

the order of Cu(111), Cu(100) to Cu(110). We note that the x and y components of the diffusion coefficient are clearly different for the interfacial water at the Cu(110) surface because of the anisotropy of the surface geometry.

The hydrogen bond lifetime correlation functions of the water molecules in the interfacial as well as in the bulk regions according to eqn (3) are plotted in Fig. 23. While the hydrogen bonds in interfacial and bulk regions have been selected using the same distance criteria as for the diffusion coefficient calculation, the auto-correlation function has been averaged for 20 ps and fitted to an exponential function. The results compiled in Table 9 show that the hydrogen bond dynamics is faster in the interfacial region compared to the bulk region and there is no pronounced difference between the investigated surfaces.

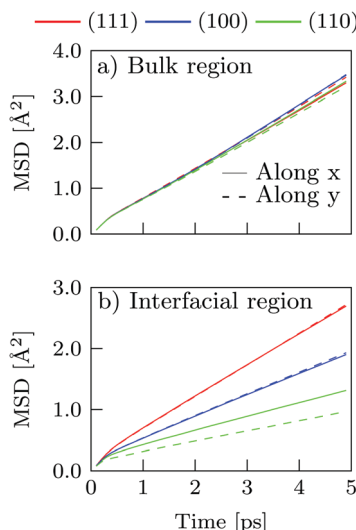


Fig. 22 Mean squared displacements (MSD) of the oxygen atoms parallel to the surfaces along the x and y directions in the bulk region (within 2.5 Å from the centre of the water film) (a) and the interfacial region (up to 5 Å from the respective surface) (b) in the Cu(111)-H₂O, Cu(100)-H₂O and Cu(110)-H₂O systems. The diffusion coefficients have been computed from the slope of a linear fit to the mean squared displacement averaged for 5 ps over 1 ns trajectories and are given in Table 9.

Finally, the residence time correlation function of the water molecules in the first peak region and those in the first hydration layer according to eqn (4) have been analysed and plotted in Fig. 24(a) and (b), respectively. Vertical distances from the surface defining the ‘well’ and ‘barrier’ regions in the first hydration layer as used for the residence lifetime calculation are listed in Table 10. The observed trend is consistent with the MSDs plotted in Fig. 22. The data in Table 9 suggests that the water molecules in the interfacial region of the Cu(110) surface reside longer compared to the Cu(100) and Cu(111) surfaces. As the surface structures become more open in the order (111) \rightarrow (100) \rightarrow (110), higher structural order of the water molecules is observed in the interfacial region. In the room temperature MD simulations that we have performed on various copper–water interfaces, spontaneous dissociation of water molecules is not observed. The absence of water

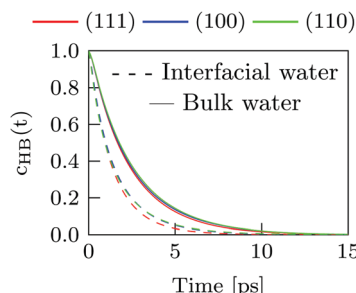


Fig. 23 Hydrogen bond life time correlation functions $c_{HB}(t)$ of water molecules in the bulk region (within 2.5 Å from the center of the water film) and in the interfacial region (up to 5 Å from the surface) of the three interfaces.

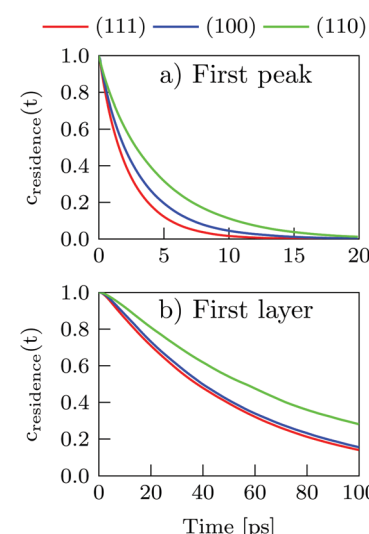


Fig. 24 Residence lifetime correlation functions ($c_{residence}(t)$) of the water molecules in the first peak region of the first hydration layer (a) and in the complete first hydration layer (b). Water molecules in both regions reside longer at the (110) surface compared to the (100) and (111) surfaces.

dissociation is not a consequence of the structures present in the training set as some structures including dissociated water molecules at the surface are included in the reference data set. It is important to note that the NN potential is in general

Table 9 Diffusion coefficients along the x (D_{xx}) and y (D_{yy}) direction, hydrogen bond lifetimes (τ_{HB}), residence lifetimes in region I (τ_I) and region I + II (τ_{I+II}) and coverage by water molecules in regions I and II for the three interfaces. The values of D have been determined by fitting a linear function to the MSD plots in Fig. 22. The lifetimes have been calculated by fitting the corresponding time correlation functions in Fig. 23 and 24 to an exponential function of type $A \times \exp\left(-\frac{t}{\tau}\right)$. The error bars for τ_{HB} and τ_I are computed by splitting the corresponding 1 ns trajectory into 5 and 9 segments of 200 ps for every 200 ps and every 100 ps, respectively and finding the maximum and minimum deviation from the mean value. Similarly for τ_{I+II} , the trajectory is split into 8 segments of 300 ps for every 100 ps

Surface	Region	D [10^{-5} cm 2 s $^{-1}$]			Coverage [%]		
		D_{xx}	D_{yy}	τ_{HB} [ps]	τ_I [ps]	τ_{I+II} [ps]	I
Cu(111)	Bulk	3.2	3.4	2.3 (+0.06/-0.07)	2.4 (+0.1/-0.2)	51.4 (+8.3/-5.0)	10.0
	Int.	2.6	2.6	1.4 (+0.04/-0.02)			41.4
Cu(100)	Bulk	3.4	3.4	2.4 (+0.14/-0.18)	3.1 (+0.5/-0.4)	53.4 (+9.5/-8.3)	17.4
	Int.	1.8	1.8	1.5 (+0.04/-0.04)			42.8
Cu(110)	Bulk	3.3	3.2	2.5 (+0.09/-0.13)	4.5 (+1.0/-1.0)	75.9 (+7.1/-9.3)	39.0
	Int.	1.2	0.9	1.5 (+0.05/-0.07)			51.0

Table 10 Vertical distances from the surface defining the ‘well’ and ‘barrier’ regions giving rise to the two peaks in the oxygen probability distribution shown in Fig. 10 and used in the calculation of residence times. $Z_{w,I}$ is defined as the center between the maximum oxygen probability in region I and the minimum between regions I and II and separates the first well at the maximum oxygen probability in region I from the barrier at the minimum. $Z_{b,I}$ corresponds to the center between the minimum and the maximum of the oxygen probability in region II and labels the transition between the first barrier region and the second oxygen peak in the first hydration layer. Similarly, $Z_{w,II}$ specifies the boundary between the peak in region II and the second barrier, which end where the oxygen probability distribution in Fig. 10 coincides with 1.0

	(111)	(100)	(110)
$Z_{w,I} [\text{\AA}]$	2.54	2.46	2.34
$Z_{b,I} [\text{\AA}]$	2.88	2.80	2.55
$Z_{w,II} [\text{\AA}]$	3.33	3.20	2.82
$Z_{b,II} [\text{\AA}]$	5.40	5.27	4.74

“reactive” like the underlying DFT reference method. This ability to describe the dissociation is a mandatory condition for studying the interaction of water with solid surfaces as the ability to dissociate and recombine is a fundamental characteristic of water.

5 Summary

A DFT-based neural network potential has been constructed for the investigation of copper–water interfaces employing a large set of bulk and interface reference structures. A very high precision has been achieved with an overall RMSE of 0.9 meV per atom for the energies and 66.5 meV per Bohr for the force components enabling simulations with essentially first-principles accuracy. The potential has first been applied to perform rigorous convergence tests concerning the required system size in terms of the water film diameter and the supercell. Several properties have been monitored for this purpose like the oxygen probability distribution along the surface normal, hydrogen bond properties and in particular the formation of a bulk-like water region in the middle of the water film. Concerning the required water film diameter, our results are consistent with a simple rule of thumb based on the assumption that interfaces modify the structure of water up to 10 Å from the surface, which is similar to the typical extension of probability fluctuations in radial distribution functions of liquid water. Consequently, in total a 40 Å water film is necessary to prevent any interaction of the most distant water molecules with the surfaces and to obtain fully bulk-like behavior.

The NN potential has then been applied to the investigation of the structural and dynamical properties of interfacial water at Cu(111), Cu(100), and Cu(110), like oxygen and hydrogen probability densities, angular orientations, hydrogen bond properties and lifetimes, diffusion coefficients and residence lifetimes. We found that the water molecules in the interfacial region, especially in the first hydration layer, are strongly influenced by the geometric structure of these surfaces. The water molecules in the first peak region of the first hydration

layer at all three interfaces prefer atop sites and are aligned close to parallel to the surface, while those in the second peak prefer more tilted configurations and show strong differences in the spatial arrangement. While the hydrogen bond lifetimes of the interfacial water molecules are very similar for all the investigated surfaces, the diffusion coefficient parallel to the surface show that the interfacial water at the Cu(111) surface is significantly more mobile than at Cu(100) and Cu(110). Related to this finding, the average residence time of the water molecules is longer at the Cu(110) surface compared to the Cu(100) and Cu(111) surfaces. This demonstrates that the structural ordering of the water molecules increases from closely packed Cu(111) surface via the Cu(100) surface to the more open Cu(110) surface. We did not observe any spontaneous dissociation of water molecules at any of the investigated surfaces although the NN potential is a reactive potential and does in principle allow to describe such events with first-principles accuracy. Our present study does only address solid–liquid interfaces in the absence of external electric fields and electrode potentials, which are important in electrochemical studies. These aspects will be addressed in future work.

Acknowledgements

This work was supported by the Cluster of Excellence RESOLV (EXC 1069) funded by the Deutsche Forschungsgemeinschaft, and the DFG projects Be3264/5-1 and Be3264/6-1 (Heisenberg fellowship JB). The authors thank Tobias Morawietz for providing the initial set of pure water geometries and Matti Hellström for discussions on correlation functions.

References

- 1 M. A. Henderson, *Surf. Sci. Rep.*, 2002, **46**, 1.
- 2 A. Verdaguer, G. M. Sacha, H. Bluhm and M. Salmeron, *Chem. Rev.*, 2006, **106**, 1478.
- 3 A. Hodgson and S. Haq, *Surf. Sci. Rep.*, 2009, **64**, 381.
- 4 F. Zaera, *Chem. Rev.*, 2012, **112**, 2920.
- 5 J. Carrasco, A. Hodgson and A. Michaelides, *Nat. Mater.*, 2012, **11**, 667.
- 6 O. Björneholm, M. H. Hansen, A. Hodgson, L.-M. Liu, D. T. Limmer, A. Michaelides, P. Pedevilla, J. Rossmeisl, H. Shen, G. Tocci, E. Tyrode, M.-M. Walz, J. Werner and H. Bluhm, *Chem. Rev.*, 2016, **116**, 7698.
- 7 S. P. Badwal, S. S. Gidley, C. Munnings, A. I. Bhatt and A. F. Hollenkamp, *Front. Chem.*, 2014, **2**, 79.
- 8 R. Ludwig, *Angew. Chem., Int. Ed.*, 2001, **40**, 1808.
- 9 D. Marx, *Science*, 2004, **303**, 634.
- 10 P. Gallo, K. Amann-Winkel, C. A. Angell, M. A. Anisimov, F. Caupin, C. Chakravarty, E. Lascaris, T. Loerting, A. Z. Panagiotopoulos and J. Russo, *et al.*, *Chem. Rev.*, 2016, **116**, 7463.
- 11 M. Ceriotti, W. Fang, P. G. Kusalik, R. H. McKenzie, A. Michaelides, M. A. Morales and T. E. Markland, *Chem. Rev.*, 2016, **116**, 7529.

- 12 H. von Helmholtz, *Ann. Phys.*, 1853, **89**, 211.
- 13 A. Hamelin, T. Vitanov, E. Sevastyanov and A. Popov, *J. Electroanal. Chem. Interfacial Electrochem.*, 1983, **145**, 225.
- 14 E. Spohr, *Electrochim. Acta*, 2003, **49**, 23.
- 15 M. Ito, *Surf. Sci. Rep.*, 2008, **63**, 329.
- 16 G. Held and D. Menzel, *Surf. Sci.*, 1994, **316**, 92.
- 17 P. J. Feibelman, *Science*, 2002, **295**, 99.
- 18 P. J. Feibelman, *Chem. Phys. Lett.*, 2004, **389**, 92.
- 19 J. Cerdá, A. Michaelides, M.-L. Bocquet, P. J. Feibelman, T. Mitsui, M. Rose, E. Fomin and M. Salmeron, *Phys. Rev. Lett.*, 2004, **93**, 116101.
- 20 A. Michaelides and K. Morgenstern, *Nat. Mater.*, 2007, **6**, 597.
- 21 J. Lee, D. C. Sorescu, K. D. Jordan and J. T. Yates Jr, *J. Phys. Chem. C*, 2008, **112**, 17672.
- 22 M. Mehlhorn, J. Carrasco, A. Michaelides and K. Morgenstern, *Phys. Rev. Lett.*, 2009, **103**, 026101.
- 23 T. Kumagai, M. Kaizu, H. Okuyama, S. Hatta, T. Aruga, I. Hamada and Y. Morikawa, *Phys. Rev. B: Condens. Matter Mater. Phys.*, 2010, **81**, 045402.
- 24 M. Forster, R. Raval, A. Hodgson, J. Carrasco and A. Michaelides, *Phys. Rev. Lett.*, 2011, **106**, 046103.
- 25 M. Mehlhorn, S. Schnur, A. Groß and K. Morgenstern, *ChemElectroChem*, 2014, **1**, 431.
- 26 D. L. Doering and T. E. Maday, *Surf. Sci.*, 1982, **123**, 305.
- 27 H. Ogasawara, B. Brena, D. Nordlund, M. Nyberg, A. Pelmenschikov, L. Pettersson and A. Nilsson, *Phys. Rev. Lett.*, 2002, **89**, 276102.
- 28 S. Nie, P. J. Feibelman, N. C. Bartelt and K. Thürmer, *Phys. Rev. Lett.*, 2010, **105**, 026102.
- 29 S. Standop, A. Redinger, M. Morgenstern, T. Michely and C. Busse, *Phys. Rev. B: Condens. Matter Mater. Phys.*, 2010, **82**, 161412.
- 30 P. J. Feibelman, N. C. Bartelt, S. Nie and K. Thürmer, *J. Chem. Phys.*, 2010, **133**, 154703.
- 31 S. Yamamoto, H. Bluhm, K. Andersson, G. Ketteler, H. Ogasawara, M. Salmeron and A. Nilsson, *J. Phys.: Condens. Matter*, 2008, **20**, 184025.
- 32 H. Keller, M. Saracino, H. M. Nguyen, T. M. T. Huynh and P. Broekmann, *J. Phys. Chem. C*, 2012, **116**, 11068.
- 33 T. Fukuma, *Sci. Technol. Adv. Mater.*, 2010, **11**, 033003.
- 34 Y. R. Shen and V. Ostroverkhov, *Chem. Rev.*, 2006, **106**, 1140.
- 35 Y. R. Shen, *J. Phys. Chem. C*, 2012, **116**, 15505.
- 36 P.-A. Mante, C.-C. Chen, Y.-C. Wen, H.-Y. Chen, S.-C. Yang, Y.-R. Huang, I.-J. Chen, Y.-W. Chen, V. Gusev and M.-J. Chen, *et al.*, *Sci. Rep.*, 2014, **4**, 6249.
- 37 D. Marx and J. Hutter, *Ab Initio Molecular Dynamics: Basic Theory and Advanced Methods*, Cambridge University Press, Cambridge, 2009.
- 38 C. Ursenbach, A. Calhoun and G. A. Voth, *J. Chem. Phys.*, 1997, **106**, 2811.
- 39 J. W. Halley, A. Mazzolo, Y. Zhou and D. Price, *J. Electroanal. Chem.*, 1998, **450**, 273.
- 40 S. Izvekov and G. Voth, *J. Chem. Phys.*, 2001, **115**, 7196.
- 41 S. Izvekov, A. Mazzolo, K. VanOpdorp and G. A. Voth, *J. Chem. Phys.*, 2001, **114**, 3248.
- 42 S. Meng, L. Xu, E. Wang and S. Gao, *Phys. Rev. Lett.*, 2002, **89**, 176104.
- 43 P. Vassilev, M. Koper and R. van Santen, *Chem. Phys. Lett.*, 2002, **359**, 337.
- 44 S. Schnur and A. Groß, *New J. Phys.*, 2009, **11**, 125003.
- 45 L.-M. Liu, C. Zhang, G. Thornton and A. Michaelides, *Phys. Rev. B: Condens. Matter Mater. Phys.*, 2010, **82**, 161415.
- 46 T. Ikeshoji, M. Otani, I. Hamada and Y. Okamoto, *Phys. Chem. Chem. Phys.*, 2011, **13**, 20223.
- 47 S. Schnur and A. Groß, *Catal. Today*, 2011, **165**, 129.
- 48 R. Nadler and J. F. Sanz, *J. Mol. Model.*, 2012, **18**, 2433.
- 49 H. J. Kulik, E. Schwegler and G. Galli, *J. Phys. Chem. Lett.*, 2012, **3**, 2653.
- 50 A. Groß, F. Gossenberger, X. H. Lin, M. Naderian, S. K. Sung and T. Roman, *J. Electrochem. Soc.*, 2014, **161**, E3015.
- 51 L. S. Pedroza, A. Poissier and M.-V. Fernández-Serra, *J. Chem. Phys.*, 2015, **142**, 034706.
- 52 L. Bellarosa, R. García-Muelas, G. Revilla-López and N. López, *ACS Cent. Sci.*, 2016, **2**, 109.
- 53 A. Kovalenko and F. Hirata, *J. Chem. Phys.*, 1999, **110**, 10095.
- 54 J. W. Halley, Y. Lin and M. Zhuang, *Faraday Discuss.*, 2002, **121**, 85.
- 55 C. D. Taylor, S. A. Wasileski, J.-S. Filhol and M. Neurock, *Phys. Rev. B: Condens. Matter Mater. Phys.*, 2006, **73**, 165402.
- 56 D. Golze, M. Iannuzzi, M.-T. Nguyen, D. Passerone and J. Hutter, *J. Chem. Theory Comput.*, 2013, **9**, 5086.
- 57 S. Sakong, M. Naderian, K. Mathew, R. G. Hennig and A. Groß, *J. Chem. Phys.*, 2015, **142**, 234107.
- 58 A. Michaelides, V. A. Ranea, P. L. de Andres and D. A. King, *Phys. Rev. Lett.*, 2003, **90**, 216102.
- 59 S. Wang, Y. Cao and P. A. Rikvold, *Phys. Rev. B: Condens. Matter Mater. Phys.*, 2004, **70**, 205410.
- 60 S. Meng, E. G. Wang and S. Gao, *Phys. Rev. B: Condens. Matter Mater. Phys.*, 2004, **69**, 195404.
- 61 B. Meyer, D. Marx, O. Dulub, U. Diebold, M. Kunat, D. Langenberg and C. Wöll, *Angew. Chem., Int. Ed.*, 2004, **43**, 6641.
- 62 O. Dulub, B. Meyer and U. Diebold, *Phys. Rev. Lett.*, 2005, **95**, 136101.
- 63 B. Meyer, H. Rabaa and D. Marx, *Phys. Chem. Chem. Phys.*, 2006, **8**, 1513.
- 64 E. Salli, J.-P. Jalkanen, K. Laasonen and L. Halonen, *Mol. Phys.*, 2007, **105**, 1271.
- 65 E. Skulason, G. S. Karlberg, J. Rossmeisl, T. Bligaard, J. Greeley, H. Jonsson and J. K. Nørskov, *Phys. Chem. Chem. Phys.*, 2007, **9**, 3241.
- 66 Q.-L. Tang and Z.-X. Chen, *Surf. Sci.*, 2007, **601**, 954.
- 67 J. Ren and S. Meng, *Phys. Rev. B: Condens. Matter Mater. Phys.*, 2008, **77**, 054110.
- 68 A. A. Phatak, W. N. Delgass, F. H. Ribeiro and W. F. Schneider, *J. Phys. Chem. C*, 2009, **113**, 7269.
- 69 P. J. Feibelman, *Nat. Mater.*, 2009, **8**, 372.
- 70 A. Belonoshko and A. Rosengren, *Langmuir*, 2010, **26**, 16267.
- 71 P. Zhang, W. T. Zheng and Q. Jiang, *J. Phys. Chem. C*, 2010, **114**, 19331.

- 72 L. Guillemot and K. Bobrov, *J. Phys. Chem. C*, 2011, **115**, 22387.
- 73 Z. Zeng and J. Greeley, *Nano Energy*, 2016, DOI: 10.1016/j.nanoen.2016.05.044.
- 74 M. W. Ribarsky, W. D. Luedtke and U. Landman, *Phys. Rev. B: Condens. Matter Mater. Phys.*, 1985, **32**, 1430.
- 75 M. Ito and M. Yamazaki, *Phys. Chem. Chem. Phys.*, 2006, **8**, 3623.
- 76 M. Mehlhorn and K. Morgenstern, *Phys. Rev. Lett.*, 2007, **99**, 246101.
- 77 T. Yamada, S. Tamamori, H. Okuyama and T. Aruga, *Phys. Rev. Lett.*, 2006, **96**, 036105.
- 78 J. Carrasco, A. Michaelides, M. Forster, S. Haq, R. Raval and A. Hodgson, *Nat. Mater.*, 2009, **8**, 427.
- 79 E. Spohr and K. Heinzinger, *Chem. Phys. Lett.*, 1986, **123**, 218.
- 80 E. Spohr, *J. Phys. Chem.*, 1989, **93**, 6171.
- 81 A. Kohlmeyer, W. Witschel and E. Spohr, *Chem. Phys.*, 1996, **213**, 211.
- 82 A. Kohlmeyer, C. Hartnig and E. Spohr, *J. Mol. Liq.*, 1998, **78**, 233.
- 83 A. Ignaczak and J. Gomes, *J. Mol. Struct.*, 1999, **464**, 227.
- 84 A. P. Willard, S. K. Reed, P. A. Madden and D. Chandler, *Faraday Discuss.*, 2009, **141**, 423.
- 85 D. T. Limmer, A. P. Willard, P. Madden and D. Chandler, *Proc. Natl. Acad. Sci. U. S. A.*, 2013, **110**, 4200.
- 86 A. C. T. van Duin, V. S. Bryantsev, M. S. Diallo, W. A. Goddard III, O. Rahaman, D. J. Doren, D. Raymand and K. Hermansson, *J. Phys. Chem. A*, 2010, **114**, 9507.
- 87 C. M. Handley and J. Behler, *Eur. Phys. J. B*, 2014, **87**, 1.
- 88 A. P. Bartók, M. C. Payne, R. Kondor and G. Csányi, *Phys. Rev. Lett.*, 2010, **104**, 136403.
- 89 J. Behler and M. Parrinello, *Phys. Rev. Lett.*, 2007, **98**, 146401.
- 90 M. Rupp, A. Tkatchenko, K. Müller and O. A. von Lilienfeld, *Phys. Rev. Lett.*, 2012, **108**, 058301.
- 91 S. Haykin, *Neural Networks and Learning Machines*, Prentice Hall, 3rd edn, 2008.
- 92 T. M. Mitchell, *Machine Learning*, McGraw-Hill, 1997.
- 93 T. B. Blank, S. D. Brown, A. W. Calhoun and D. J. Doren, *J. Chem. Phys.*, 1995, **103**, 4129.
- 94 C. M. Handley and P. L. A. Popelier, *J. Phys. Chem. A*, 2010, **114**, 3371.
- 95 J. Behler, *Phys. Chem. Chem. Phys.*, 2011, **13**, 17930.
- 96 G. Cybenko, *Math. Control Sign. Systems*, 1989, **2**, 303.
- 97 K. Hornik, M. Stinchcombe and H. White, *Neural Networks*, 1989, **2**, 359.
- 98 J. Behler, *J. Chem. Phys.*, 2011, **134**, 074106.
- 99 J. Behler, *Int. J. Quantum Chem.*, 2015, **115**, 1032.
- 100 N. Artrith and J. Behler, *Phys. Rev. B: Condens. Matter Mater. Phys.*, 2012, **85**, 045439.
- 101 K. V. Jovan Jose, N. Artrith and J. Behler, *J. Chem. Phys.*, 2012, **136**, 194111.
- 102 T. Morawietz, V. Sharma and J. Behler, *J. Chem. Phys.*, 2012, **136**, 064103.
- 103 T. Morawietz and J. Behler, *J. Phys. Chem. A*, 2013, **117**, 7356.
- 104 T. Morawietz, A. Singraber, C. Dellago and J. Behler, *Proc. Natl. Acad. Sci. U. S. A.*, 2016, **113**, 8368.
- 105 B. Cheng, J. Behler and M. Ceriotti, *J. Phys. Chem. Lett.*, 2016, **7**, 2210.
- 106 M. Hellström and J. Behler, *J. Phys. Chem. Lett.*, 2016, **7**, 3302.
- 107 J. Behler, *J. Phys.: Condens. Matter*, 2014, **26**, 183001.
- 108 G. Kresse and J. Furthmüller, *Phys. Rev. B: Condens. Matter Mater. Phys.*, 1996, **54**, 11169.
- 109 B. Hammer, L. B. Hansen and J. K. Nørskov, *Phys. Rev. B: Condens. Matter Mater. Phys.*, 1999, **59**, 7413.
- 110 P. E. Blöchl, *Phys. Rev. B: Condens. Matter Mater. Phys.*, 1994, **50**, 17953.
- 111 G. Kresse and D. Joubert, *Phys. Rev. B: Condens. Matter Mater. Phys.*, 1999, **59**, 1758.
- 112 I.-C. Lin, A. P. Seitsonen, I. Tavernelli and U. Rothlisberger, *J. Chem. Theory Comput.*, 2012, **8**, 3902.
- 113 K. Forster-Tonigold and A. Groß, *J. Chem. Phys.*, 2014, **141**, 064501.
- 114 M. D. Ben, J. Hutter and J. Vandevondele, *J. Chem. Phys.*, 2015, **143**, 054506.
- 115 I. Hamada, K. Lee and M. Yoshitada, *Phys. Rev. B: Condens. Matter Mater. Phys.*, 2010, **81**, 115452.
- 116 J. Carrasco, B. Santra, J. Klimeš and A. Michaelides, *Phys. Rev. Lett.*, 2011, **106**, 026101.
- 117 K. Tonigold and A. Groß, *J. Comput. Chem.*, 2012, **33**, 695.
- 118 J. Klimes and A. Michaelides, *J. Chem. Phys.*, 2012, **137**, 120901.
- 119 J. Carrasco, J. Klimeš and A. Michaelides, *J. Chem. Phys.*, 2013, **138**, 024708.
- 120 S. Grimme, J. Antony, S. Ehrlich and H. Krieg, *J. Chem. Phys.*, 2010, **132**, 154104.
- 121 S. Grimme, J. Antony, S. Ehrlich and H. Krieg, *DFT-D3 – A dispersion correction for density functionals, Hartree-Fock and semi-empirical quantum chemical methods*, Version 3.1 Rev. 0, 2014, <http://www.thch.uni-bonn.de/tc>.
- 122 S. Imoto, H. Forbert and D. Marx, *Phys. Chem. Chem. Phys.*, 2015, **17**, 24224.
- 123 J. Behler, *RuNNer – A neural network code for high-dimensional potential-energy surfaces*, Lehrstuhl für Theoretische Chemie, Ruhr-Universität Bochum, 2007–2016.
- 124 T. B. Blank and S. D. Brown, *J. Chemom.*, 1994, **8**, 391.
- 125 S. Plimpton, *J. Comp. Physiol.*, 1995, **117**, 1.
- 126 A. Singraber, T. Morawietz, J. Behler and C. Dellago, to be published.
- 127 S. Nosé, *J. Chem. Phys.*, 1984, **81**, 511.
- 128 W. G. Hoover, *Phys. Rev. A: At., Mol., Opt. Phys.*, 1985, **31**, 1695.
- 129 W. Shinoda, M. Shiga and M. Mikami, *Phys. Rev. B: Condens. Matter Mater. Phys.*, 2004, **69**, 134103.
- 130 M. E. Tuckerman, J. Alejandre, R. López-Rendón, A. L. Jochim and G. J. Martyna, *J. Phys. A: Math. Gen.*, 2006, **39**, 5629.
- 131 D. Laage and J. T. Hynes, *J. Phys. Chem. B*, 2008, **112**, 7697.
- 132 D. R. Lide, *CRC handbook of chemistry and physics*, CRC press, 2009.
- 133 G. I. Csonka, J. P. Perdew, A. Ruzsinszky, P. H. T. Philipsen, S. Lebegue, J. Paier, O. A. Vydrov and J. G. Angyan, *Phys. Rev. B: Condens. Matter Mater. Phys.*, 2009, **79**, 155107.

- 134 M. Beg and S. Shapiro, *Phys. Rev. B: Condens. Matter Mater. Phys.*, 1976, **13**, 1728.
- 135 C. Kittel, *Introduction to solid state physics*, John Wiley & Sons, Inc., 2005.
- 136 K. Röttger, A. Endriss, J. Ihringer, S. Doyle and W. Kuhs, *Acta Crystallogr., Sect. B: Struct. Sci.*, 1994, **50**, 644.
- 137 E. Whalley, *J. Chem. Phys.*, 1984, **81**, 4087.
- 138 W. Wagner and A. Prüß, *J. Phys. Chem. Ref. Data*, 2002, **31**, 387.
- 139 P. Tofts, D. Lloyd, C. Clark, G. Barker, G. Parker, P. McConville, C. Baldock and J. Pope, *Magn. Reson. Med.*, 2000, **43**, 368.
- 140 A. K. Soper, *ISRN Phys. Chem.*, 2013, **2013**, 279463.